Experimental characterization of radiative transfer in semi-transparent composite materials with rough boundaries

Florent Retailleau, Vadim Allheily, Lionel Merlat, Jean-François Henry, Jaona Harifidy Randrianalisoa

Version of Record: https://www.sciencedirect.com/science/article/pii/S0022407320304301
Manuscript_8876ce26aba8faf4032a7d686cb8b36d

Experimental characterization of radiative transfer in semi-transparent composite materials with rough boundaries

Florent Retailleau[a,b,*], Vadim Allheily[a], Lionel Merlat[a], Jean-François Henry[b], Jaona Randrianalisoa[b,*]

[a] *French-German Research Institute of Saint-Louis (ISL), 5 rue du Général Cassagnou, BP 70034, 68301 Saint-Louis CEDEX, France*
[b] *Institut de Thermique, Mécanique, Matériaux (ITheMM), EA 4694, Université de Reims Champagne-Ardenne, Campus du Moulin de la Housse, F-51687, Reims, France*

Abstract

This study deals with the analysis of the propagation of thermal radiation within absorbing and scattering composite materials with rough boundaries. The two-phase system (resin matrix and fibers reinforcement) is treated as an equivalent homogeneous medium characterized by volumetric radiative properties, namely extinction coefficient, scattering albedo, and phase function whereas the interaction of the radiation with the medium boundaries is modeled with boundary scattering properties. The aim is to determine these volumetric and boundary scattering properties by an inverse analysis for parameter identification. It consists of minimizing the sum of the squared difference between calculated and measured bidirectional and normal-hemispherical reflectances and transmittances. The Gauss–Newton algorithm is employed for solving this nonlinear least squares problem. The experimental data are obtained by using a visible and near-infrared spectrophotometer equipped with a goniometric system enabling measurements in different scattering directions around a sample between 0.4 and 2.5 μm. The collision-based Monte Carlo method is employed to assess the theoretical values by solving the Radiative Transfer Equation (RTE) along with boundary conditions designed for samples with rough surfaces. The proposed approach is proved to be well appropriate for determining the radiative properties of the rough composite samples. More interestingly, this study demonstrates that the scattering phase function can be modeled by the Henyey and Greenstein approximation and the boundary scattering distributions can be modeled by a Gaussian function and/or a cosine function.

1. Introduction

Composite materials are today involved in many engineering applications due to to their unique structural features namely, lightness, solidity and rigidity and their competitive production costs. In various applications, such as automotive, building, aerospace, and defense, light or laser radiation constitutes a tool for a non-destructive characterization, remote sensing, and diagnostic of materials and structures. A better understanding of the light propagation within composite materials, an absorbing-scattering medium characterized by optically rough surfaces, is very important for developing such light analysis-based devices.

Many studies have been reported on radiative transfer in absorbing and scattering semi-transparent media [1–4]. Special attention has been paid to high porosity materials such as foams [2, 5–10], fibrous media [3, 11–22] low porosity materials such as silica aerogel [23], glass containing bubbles [24] and porous ceramics manufactured from partial sintering of powder compact [1, 25, 26]. In most of these studies, the material boundaries are treated either entirely transparent (in the case of foams and fibrous materials) or optically smooth (in the case of low porous materials). The radiative transfer in composite materials has been subjected to a limited amount of investigations. Existing studies have been mainly focused on polymers loaded with glass, ceramic or metallic particles for radiative cooling [27–30], new ablative materials of thermal protection systems [31], and solar energy applications [32–34]. The present study deals specifically with the radiative transfer in structural composite materials characterized by woven reinforcements. One of the challenges in

*Corresponding author:
Email addresses: florentretailleau.1@gmail.com (Florent Retailleau), jaona.randrianalisoa@univ-reims.fr (Jaona Randrianalisoa)

studying the radiative transfer in composite materials is the presence of rough boundaries resulting from the manufacturing process. The presence of rough boundaries is difficult to handle from a theoretical point of view while the boundary scattering may significantly affect the radiative transfer and specifically light scattering measurements.

The exact solution of light propagation in semi-transparent media can be obtained from the electromagnetic theory [35, 36]. However, this rigorous approach is computationally demanding and, for instance, is not applicable to heterogeneous media with heterogeneity sizes greater than the wavelength. Alternatively, the radiative transfer theory can be employed [37–39]. In this theory, the propagation of the radiation intensity through the medium is described by the Radiative Transfer Equation (RTE). When heterogeneities are much larger than the wavelength, two RTE-based approaches can be employed: the discrete-scale and the continuum approaches. The former applies the RTE through the discrete heterogeneous material, e.g. a sample reconstructed from X-ray micro-tomography technique, while the later replaces the real material by a single-homogeneous or a multiple-homogeneous phase medium characterized by the so-called radiative properties [40, 41]. Clearly, the discrete scale approach involves fewer approximations but a higher computational cost. Usually, it is restricted to provide a reference solution.

In the framework of the continuum approach, the radiative transfer problem in heterogeneous media is generally modeled by the single-homogeneous phase approximation (HPA) through a single-RTE. This approach may be questionable in some situations such as very fast processes and in the presence of chemical reactions for which non-equilibrium heat transfer prevails between different phases of the medium. In those cases, the multiple-homogeneous phase (MPA) or multi-RTE approximation based continuum model can be used [40, 41]. The multi-RTE approach is better than the single-RTE model to describe the radiation intensity propagation in multiphase systems. However, it involves a large number of mostly unknown radiative properties, which makes the radiative transfer problem more challenging.

Studying the radiative transfer in heterogeneous media involve two aspects: finding the solution of the RTE on the one hand and determining the radiative properties on the other hand. In the case of heterogeneous media with rough boundaries such as composite materials, the intensity propagation is characterized by the volumetric radiative properties (absorption coefficient, scattering coefficient and scattering phase function) and the surface scattering properties (reflectivities and transmittivities). Several numerical methods have been developed to solve the RTE. Some of the current popular methods to solve the RTE are the spherical harmonics [42], the discrete ordinate method (DOM) [43], the finite volume method [44], the finite element method [45], the zone method [46] and the Monte Carlo (MC) method [47, 48]. Each of these methods has its own advantages and drawbacks [38]. Selecting the right resolving method depends essentially on the trade-off between implementation effort, computation cost, and accuracy. The stochastic MC method is time consuming compared to deterministic methods however, it is far better to handle complex physical processes and multidimensional problems. In this work, the MC method is chosen to solve the RTE where the computation time is shown to be acceptable.

The radiative volumetric properties can be determined either by the use of a theoretical model based on Maxwell's equations solution for isolated particles such as the Mie theory, geometric optics and the diffraction theory [49] or an inverse analysis for parameter identification based on the solution method of the RTE and spectrometric transmittance and reflectance measurements [50]. Baillis and Sacadura [51] recommend the first method in the case of simple scatterer geometry and the second one for more complex dispersed materials such as foam, porous ceramic and fibrous media. The ray tracing-based numerical model has attracted much attention these recent years [41, 50, 52–54] but such model is only applicable to heterogeneous media in the limit of geometric optics, which is not the case of current composite materials. As shown in the work of Hale and Bohn [55], the identification of radiative properties is carried out from hemispherical reflectance and transmittance measurements. In their works, Kuhn et al. [56] use a similar experimental method but with measurements on samples of different thicknesses in order to further retrieve the scattering phase function consisting of two unknown parameters. In order to identify the extinction coefficient, the albedo and the phase function of fibrous insulating materials, Nicolau et al. [57] and Henry et al. [58] use bidirectional transmittance and reflectance measurements. The bidirectional-based measurements were employed by other researchers such as Randrianalisoa et al. [24] and later Coray et al. [59] to identify radiative properties of other heterogeneous media. Note that the determination of the exact scattering phase function needs the use of a complex function such as series of Legendre polynomials involving a larger number of unknown parameters, which makes the inverse method of identification challenging. In the early works of

Nicolau et al. [57], an alternative approach to the complex scattering phase function uses a combination of simple scattering functions such as the Henyey and Greenstein approximation and isotropic functions. The bidirectional-based measurements enable to retrieve a large number of radiative parameters compared to the hemispherical-based measurements but require specific detection devices such as a high sensitivity detector mounted on a goniometric system. The combination of hemispherical and bidirectional measurements enables increasing the number of measurements [60] while ensuring accurate retrieval of hemispherical transmittance and reflectance data.

In all the previous studies, the sample boundaries are simplified as transparent or optically smooth by following the Fresnel's laws of reflection and refraction. Consequently, their theoretical models are not directly applicable to composite materials due to the presence of rough boundaries. Specifically, the scattering of the incident radiation caused by the rough boundaries induces a drastic change of radiation penetrating/leaving the sample.

The reflection of electromagnetic waves from a rough surface was introduced by Davis in 1954 [61]. Then, several studies have been focused on the scattering behavior of an incident light on perfectly reflecting or opaque rough surfaces [62–64]. However, the methods developed in these works are only valid in the context of geometric optics for opaque surfaces. The light interaction on rough surfaces is also a common concern in the field of photovoltaic cells. One of the methods developed in this field consists in solving Maxwell's equations. The electromagnetic field is determined throughout the entire space and takes into account the exact surface topography [65, 66]. Rather than using this complex electromagnetic method, a semi-empirical approach has often been recommended [34, 67]. With this alternative method, the diffuse reflection and transmission of light are either obtained from experiments or modeled by the Lambert cosine law. However, in almost all the studies related to photovoltaic cells, there is no volumetric scattering within the medium. More recently, the Monte Carlo method has been used to model the distribution of reflected rays on metallic surfaces [68] but also on semi-transparent sample incorporating both surface and volumetric scattering [69].

Our work aims to improve the current knowledge in the field of radiative properties characterization of dispersed media. Specifically, the objective is to simultaneously determine the volumetric radiative properties and the surface scattering properties of rough composite materials made of woven fibers reinforcements and resin matrix. An inverse analysis for parameter identification using the Gauss–Newton algorithm is employed. The principle is to minimize the sum of the squared difference between calculated and measured bidirectional and normal-hemispherical reflectances and transmittances.

In the following, the investigated materials are first described. Then, the inverse method for parameter identification is recalled. After, the direct model based on stochastic MC solution method of the RTE and the experimental device to acquire the bidirectional and normal-hemispherical transmittances and reflectances are detailed. Finally, the results are presented and discussed.

2. Materials and characterizations

2.1. Materials

The materials investigated in this study are laminated composites made of an epoxy resin and fiberglass reinforcements. This type of material is typically employed in aeronautics and specifically for aircraft structures. Laminate composite structures consist of successive reinforcing layers impregnated with a polymer resin. The orientation of each layer is a key variable: in this study, plies are alternatively oriented at 0 or 90° and the stacking sequence is symmetrical to the median plane. The final curing is accomplished by the simultaneous application of heat and pressure. At the end, the reinforcements give a high mechanical strength to the material while the resin provides cohesion between the fibers and spreads the mechanical stresses throughout the system. In this study, the samples are made of 4, 8 and 16 plies, which correspond to a thickness of 0.76 mm, 1.50 mm and 3.60 mm, respectively.

The epoxy resin (M10R type) represents about 43% of the mass of the composite material. The refractive index of this resin in the visible spectrum is between 1.49 and 1.58. E-glass type glass fibers present a density of 2.56 g/cm^3 and a refractive index of approximately 1.6. The finished composite samples are obtained from an industrial prepreg (ref. HexPly® Draft M10R/43%/823) from Hexcel Company which is compressed and heated inside an autoclave. Detailed informations about the samples are not available for confidentiality reasons.

2.2. Characterization

We employed an X-ray micro-computed tomography (μ-CT) imaging to have internal details of the samples. The μ-CT was done by using a vjtomejx, GE Sensing and Inspection Technologies Phoenix Xjray, 160 kV, with a resolution of 5 μm. Figure 1 depicts a two-dimensional grayscale photograph of a 8 plies sample consisting of 810 pixels by 780 pixels showing the morphology and arrangement of the reinforcements. The fiber orientation is alternated to produce a cross-ply laminate. Each fiber strand consists of a multitude of cylindrical glass fibers with a diameter within the micrometer range. One can further observe some very dark areas on the figure, they probably correspond to air cavities and show that the composite samples exhibit micro porosity (pore size on the order of micrometer), which arises due to the incomplete impregnation of the resin. Figure 2 shows a three-dimensional (3D) rendering of the 8 plies sample. These images make clear that radiation beams traveling through such a material undergo multiple interactions due to the heterogeneities (fibers and micro porosities) as they travel through the material.

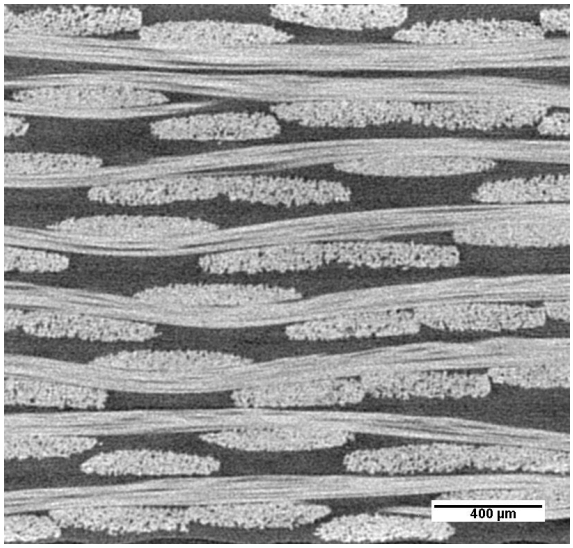

Figure 1: X-ray tomography scan of a 8 plies glass-epoxy composite sample of 810 pixels x 780 pixels.

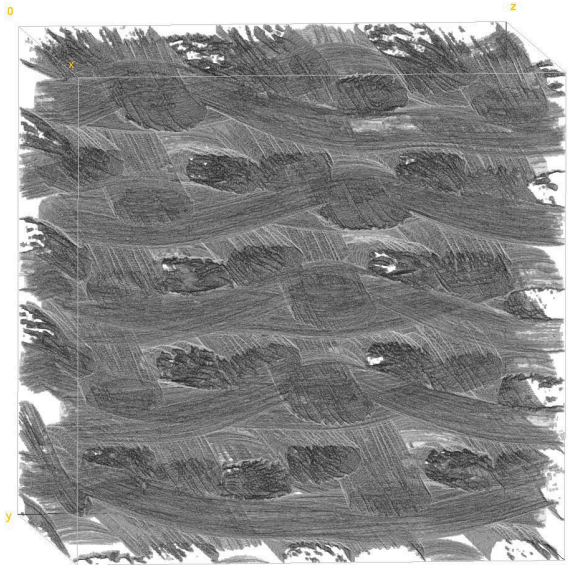

Figure 2: 3D rendering of a 8 plies glass-epoxy sample obtained from x-ray computed tomography imaging. The image dimensions are 500 x 500 x 500 voxels.

3. Method

3.1. Theoretical model

The theoretical model is based on the single-RTE approach. In this study, the semi-transparent medium is considered to be cold (without any self-emission) and homogeneous. The RTE along a line of sight is then written in the following form [38, 48]:

$$\frac{\partial I_\lambda(s,\theta,\varphi)}{\partial s} = -(\kappa_\lambda + \sigma_\lambda) I_\lambda(s,\theta,\varphi) + \frac{\sigma_\lambda}{4\pi} \int_0^{4\pi} \Phi_\lambda(\theta,\varphi,\theta',\varphi') I_\lambda(s,\theta',\varphi') \mathrm{d}\omega' \tag{1}$$

with $I_\lambda(s,\theta,\varphi)$ the spectral intensity at the abscissa s along the direction characterized by the couple of angles (θ,φ) with θ the polar angle and φ the azimuthal angle, $d\omega' = sin\theta' d\theta' d\varphi'$ the unit solid angle, κ_λ the absorption coefficient, σ_λ the scattering coefficient. The phase function Φ_λ is approximated here by the Henyey and Greenstein function where g_λ is the asymmetry factor [38]:

$$\Phi_\lambda = \frac{1 - g_\lambda^2}{(1 + g_\lambda^2 - 2 g_\lambda cos\gamma)^{3/2}} \tag{2}$$

γ is the angle between the direction of the ray before a scattering event and the direction after the scattering event. The extinction coefficient which describes the rate of attenuation of the radiation per distance unit β_λ and the albedo ω_λ which gives the probability of scattering of a beam, are linked to the absorption and scattering coefficient as follows:

$$\beta_\lambda = \kappa_\lambda + \sigma_\lambda \tag{3}$$

$$\omega_\lambda = \frac{\sigma_\lambda}{\kappa_\lambda + \sigma_\lambda} \tag{4}$$

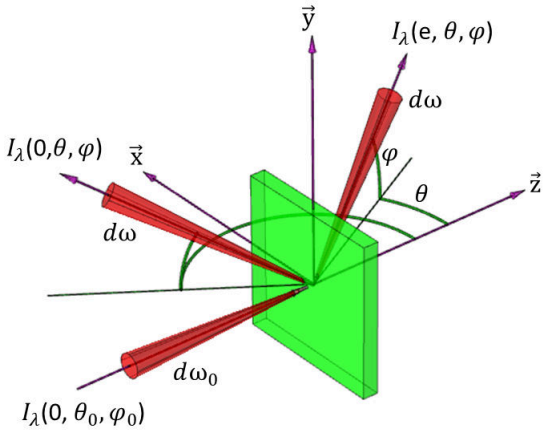

Figure 3: Representation of bidirectional transmittance and reflectance.

The boundary conditions describe the spectral intensity leaving the boundaries into the medium with $\mu = cos\theta$. The system is considered to be semi-infinite along the x and y of the Cartesian reference and hypothesis of azimuthal symmetry is adopted. The suitability of this hypothesis was analysed by comparing the hemispherical measurements obtained with an integrating sphere and the hemispherical data obtained from the bidirectional measurements (Eqs. 32 and 33) as reported in the appendix A.1.3. The boundary conditions for a collimated irradiation impinging on the sample plane boundary at the abscissa $s_0 = (x, y, z = 0)$ are given by:

$$I(s_0,\theta,\varphi) = (1 - r_{12}(\mu_0,\mu))I(s_0,\theta_0,\varphi_0) + \int_0^{2\pi}\int_0^1 r_{21}(\mu',\mu)I(s_0,\theta'\varphi')\mu' d\mu' d\varphi',\ 0 \le \theta < \frac{\pi}{2}, \theta' = cos^{-1}\mu' + \frac{\pi}{2} \tag{5}$$

$$I(s_e,\theta,\varphi) = \int_0^{2\pi}\int_0^1 r_{21}(\mu',\mu)I(s_e,\theta',\varphi')\mu' d\mu' d\varphi',\quad \frac{\pi}{2} < \theta \le \pi, \theta' = cos^{-1}\mu' \tag{6}$$

with $s_e = (x, y, z = e)$ the coordinate of the opposite boundary, normal to the z-axis of the Cartesian reference and e the sample thickness. The radiation intensities leaving the medium are determined as follows:

$$I(s_0,\theta,\varphi) = r_{12}(\mu_0,\mu)I(s_0,\theta_0,\varphi_0) + \int_0^{2\pi}\int_0^1 (1 - r_{21}(\mu',\mu))I(s_0,\theta',\varphi')\mu' d\mu' d\varphi',\ \frac{\pi}{2} < \theta \le \pi, \theta' = cos^{-1}\mu' + \frac{\pi}{2} \tag{7}$$

$$I(s_e,\theta,\varphi) = \int_0^{2\pi}\int_0^1 (1 - r_{21}(\mu',\mu))I(s_e,\theta',\varphi')\mu' d\mu' d\varphi',\quad 0 < \theta \le \frac{\pi}{2}, \theta' = cos^{-1}\mu' \tag{8}$$

$r_{21}(\mu',\mu)$ refers to the reflectivity for an incident beam in the medium of index i along the direction of cosine μ' reflected into the direction of cosine μ by the interface between the medium i and medium j.
The bidirectional reflectance/transmittance (ρ"/τ") describe the intensity of the radiation reflected/transmitted by the medium at coordinate s_0/s_e along a direction of angles θ and φ, normalized by the incident flux.

$$\rho"(\theta,\varphi) = \frac{I(s_0,\theta,\varphi)}{I_0\mu_0 d\omega_0},\quad \mu = cos\theta, \frac{\pi}{2} < \theta \le \pi \tag{9}$$

$$\tau"(\theta,\varphi) = \frac{I(s_e,\theta,\varphi)}{I_0\mu_0 d\omega_0}, \quad \mu = cos\theta, 0 \leq \theta < \frac{\pi}{2} \tag{10}$$

$I_0\mu_0 d\omega_0$ is the incident light flux in the absence of the sample. $I_0 = I(s_0,\theta_0,\varphi_0)$ refers to the intensity of the incident beam. $d\omega_0$ is the solid angle of the incident flux, and $\mu_0 = 1$ and $\varphi_0 = 0$ for a beam normally incident on the sample surface. The azimuthal symmetry hypothesis along with normal incident flux condition makes the solution of the problem invariant around the z-axis. Therefore, the reference to the angle φ is omitted hereafter for simplicity reason and we will use the following simplification rule: $\rho"(\theta) = \rho"(\theta,\varphi)$ and $\tau"(\theta) = \tau"(\theta,\varphi)$.

For rough boundaries, the Fresnel equations alone are not correct to determine the reflectivities involved in Eqs. (5) to (8). One of the solutions employed in the literature, and more particularly in the field of photovoltaic cells, is to use a semi-empirical model [34, 67]. It is assumed that the physics of the reflection at the interface between two media are decoupled from each other [70, 71]. Under such hypothesis, the angular reflection distribution, the reflection strength and the angle dependence of the incident light and reflected light are modeled by three distinct terms. The reflectivity of an interface between medium i and medium j, $r_{ij}(\mu',\mu)$ is thus expressed as follows:

$$r_{ij}(\mu',\mu) = R_{ij}(\mu')p(\mu)Cf_{ij} \tag{11}$$

$R_{ij}(\mu')$ is the reflectivity for a smooth interface calculated with Fresnel equations and is function of the incidence angle and the refractive indexes of the two adjacent media. $p(\mu)$ is a probability distribution function for an arbitrary incident beam to be reflected into the direction of cosine μ. Based on experimental observations, the probability distribution function has been modeled by the cosine law, Eq. (12) [39], or a Gaussian function, Eq. (13) [72]. The choice between these two functions is made to better reproduce the experimental data and will be discussed in the results section.

$$p(\mu) = \mu \tag{12}$$

$$p(\mu) = e^{\frac{-(cos^{-1}\mu)^2}{2\sigma_G^2}} \tag{13}$$

with σ_G the standard deviation of the Gaussian function.

In Eq. (11), Cf_{ij} is a reflectivity factor that aims to correct the Fresnel reflectivity R_{ij} due to the rough nature of the surface. This factor assesses the size of the roughness of the interface relative to the wavelength λ of the beam. It can be expressed theoretically as follows [71]:

$$Cf_{ij} = e^{-\frac{1}{2}(\frac{2\pi Ra(n_i - n_j)}{\lambda})^2} \tag{14}$$

With n_i and n_j the refraction indexes of the medium i and the medium j, respectively, and Ra the root-mean-square of the roughness. For an ideally smooth surface, the roughness $Ra = 0$, the correction factor Cf_{ij} is equal to 1 according to Eq. (14). At the same time, the probability distribution function of reflected radiation should include, contrary to Eqs. (12) and (13), a dependence on both incident and reflection directions in the following form: $p(\mu',\mu) = 1$ if $\mu' = -\mu$ and $p(\mu',\mu) = 0$ otherwise. Unfortunately, the roughness Ra alone is insufficient to describe completely the roughness of a surface. This parameter does not take into account the frequency of the peaks and therefore the slope of the roughness. In addition, the roughness Ra gives no information about the second order superimposed on the basic roughness [38]. As an alternative approach to Eq. (14), this correction factor has been determined by adjusting its value in order to better produce the measurements [71]. The radiation model described above involves six unknown parameters, namely the extinction coefficient β_λ, the scattering albedo ω_λ, the asymmetry parameter g_λ of the Henyey and Greenstein phase function and the three boundary scattering parameters Cf_{21}, Cf_{12} and σ_G.

3.2. Monte Carlo simulation

In order to solve the RTE, Eq. (1), along with boundary conditions, Eqs. (5) and (6), a collision-based MC method is employed. This method is well suitable to radiative transfer problems, as shown by Fleck [47] and later by Howell and Perlmutter [48]. It does not involve any mathematical simplification, which thus leads to a reference solution.

Briefly, MC simulation consists to individually trace the propagation of N photon bundles, also referred as rays, which interact with the absorbing and scattering medium. A ray is characterized by its position, wavelength, and direction during its propagation throughout the medium. To have an overview of the implemented MC simulation, a flowchart is provided in Figure 4. Each new ray is launched normally to the boundary ($\mu = 1$) at the abscissa $z = 0$. It may be reflected back or transmitted in the medium according to the following test. The ray is transmitted in and enters the medium if:

$$\xi_{r12} > R_{12}(1)Cf_{12} \tag{15}$$

Otherwise, the ray is reflected and contributes to the reflectance. A counter of reflected rays into the direction of cosine μ, $N_r(\mu)$, is updated and a new ray is launched. Usually, the ray direction is characterized by the polar θ and the azimuth angles φ with $\mu = cos\theta$. Therefore, the direction of the reflected ray is determined by solving Eq. (16).

$$\xi_{r,\mu} = \frac{\int_{\mu}^{0} p(|\mu'|)d\mu'}{\int_{-1}^{0} p(|\mu'|)d\mu'} \qquad \text{and} \qquad \varphi = 2\pi\xi_{r,\varphi} \tag{16}$$

with $p(\mu)$ the probability of boundary scattering defined by Eq. (12) or (13) and $\xi_{r,\mu}$ and $\xi_{r,\varphi}$ two different random numbers drawn uniformly between 0 and 1. The direction of the transmitted ray into the medium of polar angle cosine μ and azimuth angle φ is determined in a similar way as reflected rays according to Eq. (17) using two different new random numbers $\xi_{t,\mu}$ and $\xi_{t,\varphi}$.

$$\xi_{t,\mu} = \frac{\int_{0}^{\mu} p(|\mu'|)d\mu'}{\int_{0}^{1} p(|\mu'|)d\mu'} \qquad \text{and} \qquad \varphi = 2\pi\xi_{t,\varphi} \tag{17}$$

Inside the medium, the distance that the ray will travel before undergoing extinction is given by:

$$\Lambda = -\frac{ln(\xi)}{\beta_{\lambda}} \tag{18}$$

At the extinction location, the following condition is checked to decide on the future of the ray.

$$\xi > \omega_{\lambda} \tag{19}$$

If this inequality is satisfied, the ray is absorbed, a counter of absorbed rays N_a is updated and a new ray is launched. Otherwise the ray undergoes scattering and the ray direction is changed by solving the equation below based on the Henyey and Greenstein phase function and using new random numbers ξ_{μ} and ξ_{φ}.

$$\mu = \frac{1}{2g}\left[1 + g^2 - \left(\frac{1-g^2}{1-g+2g\xi_{\mu}}\right)^2\right] \qquad \text{and} \qquad \varphi = 2\pi\xi_{\varphi} \tag{20}$$

When the ray interacts with the internal side of the boundary, it may be transmitted out or reflected in the medium according to the following test. The ray is reflected back if the next condition is verified by means of a new random number ξ_{r21}.

$$\xi_{r21} < R_{21}(\mu)Cf_{21} \tag{21}$$

In such a case, the reflected ray direction is defined by Eq. (16) and the ray continues its propagation in the medium until it is either absorbed in or exits from boundaries. If the inequality, Eq. (21), is not true, the ray leaves the medium from one of the two boundaries and a new ray is launched. When the exit boundary is located at the abscissa $z = 0$, the ray contributes to reflectances. The direction cosine of the ray μ is again determined by Eq. (16) and the number of reflected rays into this direction $N_r(\mu)$ is updated. Now, when the exit boundary is located at $z = e$, the ray contributes to transmittances, its direction is computed through Eq. (17) and a number of transmitted rays $N_t(\mu)$ is updated.

The sum of $N_r(\mu)$ over all backward directions ($-1 \leq \mu < 0$) divided by the total number of rays N represents the normal-hemispherical reflectance. Similarly, the sum of $N_t(\mu)$ over all forward directions ($-1 \leq \mu < 0$) divided by the total number of rays N represents the normal-hemispherical transmittance of the sample, respectively.

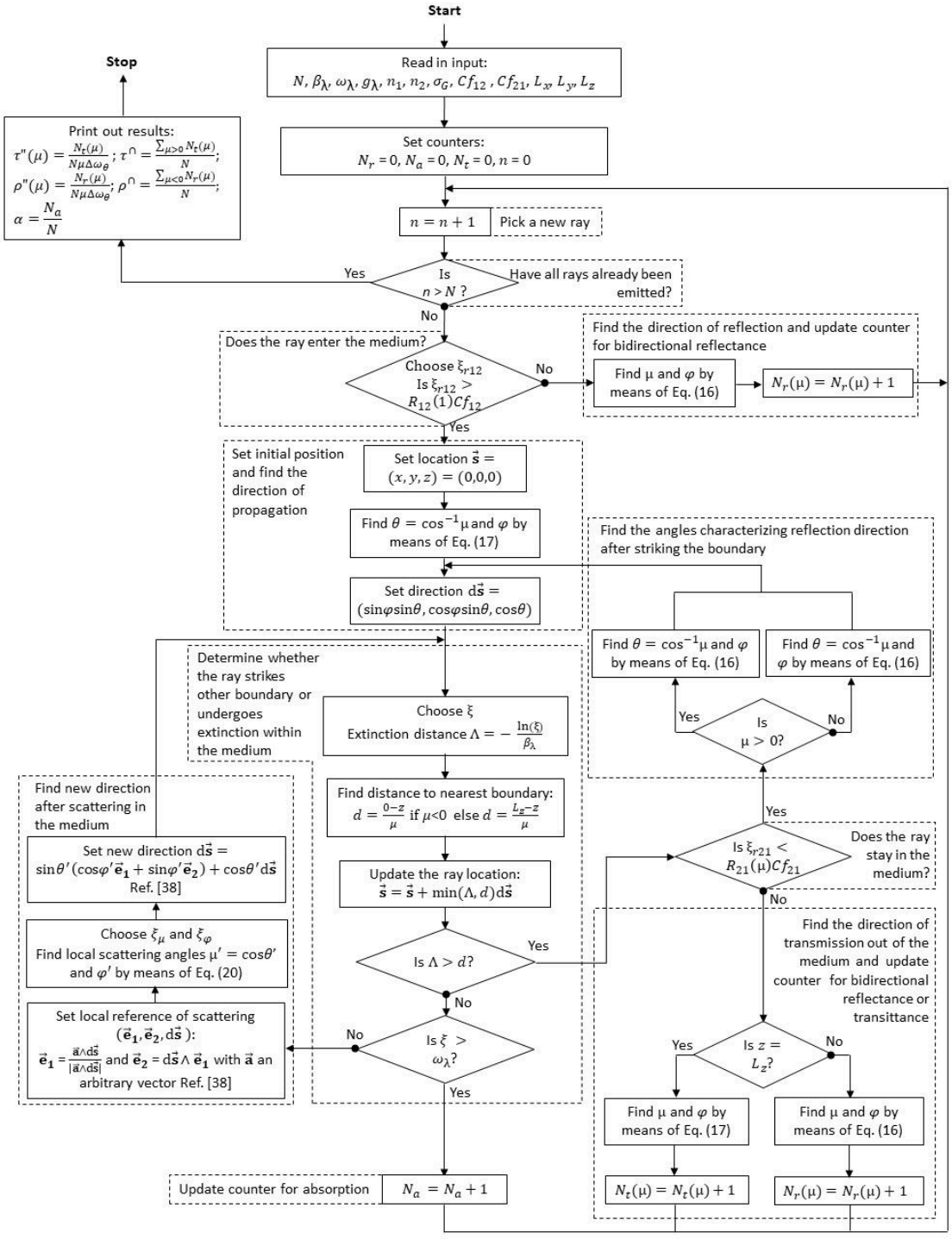

Figure 4: Flowchart for Monte Carlo solution of ray propagation in an absorbing, scattering and cold medium with semi-transparent rough boundaries.

The bidirectional transmittance or reflectance can be expressed as the number of rays leaving the sample along a direction of cosine $\mu = cos\theta$ within a differential solid angle $\Delta\omega_\theta$.

$$\rho''(\theta) = \frac{N_r(\mu)}{N\mu\Delta\omega_\theta} \tag{22}$$

$$\tau"(\theta) = \frac{N_t(\mu)}{N\mu\Delta\omega_\theta} \tag{23}$$

With N the total number of rays and $\Delta\omega_\theta$ the elementary solid angle containing all rays in the direction of angle θ and defined as follows [73]

$$\Delta\omega_\theta = 2\pi \int_{\mu_{max}}^{\mu_{min}} d\mu = 2\pi(\mu_{min} - \mu_{max}) \quad \text{for} \quad 0 \leq \theta < \pi/2 \tag{24}$$

$$\Delta\omega_\theta = \Delta\omega_{\pi-\theta} \quad \text{for} \quad \pi/2 \leq \theta \leq \pi \tag{25}$$

The bounds of integration in Eq. (24) follow the rules:

$$\mu_{min} = \begin{cases} cos(\theta - \Delta\theta/2), & \text{for} \quad 0 < \theta < (\pi/2 - \Delta\theta/2) \\ 1, & \text{for} \quad \theta = 0 \end{cases} \tag{26}$$

and

$$\mu_{max} = \begin{cases} cos(\theta + \Delta\theta/2), & \text{for} \quad 0 < \theta < (\pi/2 - \Delta\theta/2) \\ 0, & \text{for} \quad \theta = \pi/2 - \Delta\theta/2 \end{cases} \tag{27}$$

$\Delta\theta$ is the angular interval of discretization and is taken equal to the measurement angular interval (i.e. 5°). In order to assess the suitability of the implemented MC simulation, verification tests were performed. The details of these tests are reported in appendix A.2.

3.3. Experimental method

3.3.1. Experimental setup

The identification method requires some robust measurement data, which mostly condition the quality and the significance of the retrieved parameters. The hemispherical reflectance and transmittance data are easy to obtain with the use of an integrating sphere and a photo-detector coupled to a monochromatic light source or a spectrometer. Bidirectional measurements are more challenging. They require a high sensitivity detector and an accurate goniometer system. In this study, the Agilent Cary Universal Measurement Accessory (UMA) attached to the Agilent Cary 7000 Universal Measurement Spectrophotometer was used. The light source was a deuterium lamp with a spectral range between 400 and 2500 nm with a resolution of 0.4 nm. The spectrophotometer was equipped with two detectors, a Silicon and an InGaAs. The goniometer could turn around a vertical axis from 0° to 168° with an accuracy of 0.02°. The sample holder could also pivot around the same axis enabling measurement of the specular reflection, e.g. at the scattering angle of 168° to 180°.

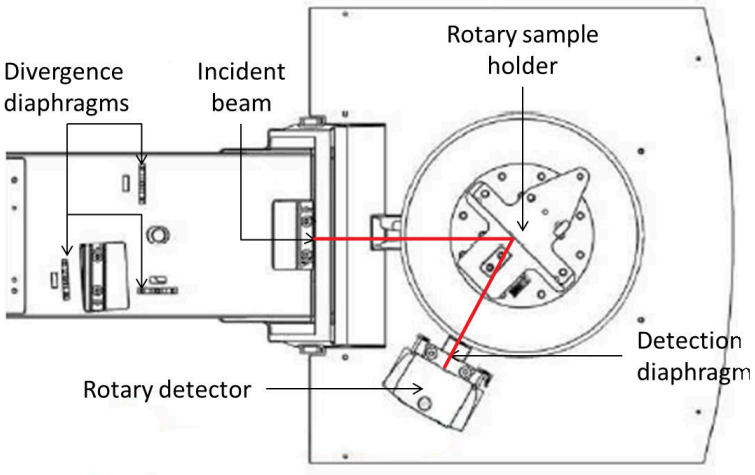

Figure 5: Agilent Cary Universal Measurement Accessory. The red line show the optical path for specular reflection measurements.

The spectrophotometer returns a signal ratio $M(\theta)$ such as [24, 57]:

$$M(\theta) = \frac{I(\theta) cos\theta d\omega_d}{I_0 min(d\omega_d, d\omega_0)} \tag{28}$$

With $d\omega_d$ the solid angle of detection linked to the irradiated area of the sensor. Since the incident beam is not perfectly collimated, it is also essential to consider the solid angle of divergence $d\omega_0$ in order to calculate the bidirectional transmittances and reflectances. From Eqs. (9), (10) and (28), it is possible to calculate the values of bidirectional transmittances and reflectances as follows [24, 57]:

$$\rho"(\theta), \tau"(\theta) = \frac{M(\theta)}{cos\theta max(d\omega_d, d\omega_0)} \tag{29}$$

The solid angles $d\omega_0$ and $d\omega_d$ were controlled with two diaphragms, respectively positioned upstream and downstream of the sample. The diaphragm positioned upstream of the sample enabled to fix the divergence angle of the incident beam. Small diaphragm and consequently a small divergence angle would provide a quasi-collimated incident beam. However, such a setup strongly attenuates the amount of signal resulting in a greater measurement noise. The choice of diaphragm was based on the absorbing and/or scattering nature of the sample. The solid angle $d\omega_0$ can be calculated as follows:

$$d\omega_0 = 2\pi(1 - cos\Theta_0) \tag{30}$$

with Θ_0 the diaphragm opening angle.

The detection diaphragm enabled the control of the solid angle of detection $d\omega_d$, which is also calculated with Eq. (30) but with Θ_d the opening angle of the diaphragm. The choice of the detection diaphragm influences the measurement quadrature. The measurement discretization angle should be greater than the diaphragm opening angle Θ_d to avoid double counting of the signal coming from the previous measurement angle.

The measurement was carried out on the horizontal plane every 5°, from 0° to 85° for the bidirectional transmittances and from 95° to 180° for the bidirectional reflectances. The choice of using a 5° discretization angle enabled a large number of measurements while avoiding the overlapping of the measurements due to the divergence of the incident beam and the detector solid angle. Unlike other discretizations which favor measurements around the forward direction 0° and backward direction 180° [57], due to the forward and backward behavior of the scattering, here the high sensitivity of the detector and the broad scattering behavior of the samples enabled scanning the entire hemisphere. Reflectance measurement beyond 165° cannot be realized because, under this configuration, the detector hides the incident beam directed at the sample (see Figure 6a). To carry out the reflectance measurements for scattering angles between 170° and 180°, it is a common practice to tilt the sample by a small angle [24, 57, 58]. This tilt angle is about 6.5° in the present study according to Figure 6.b. Note that the inclination of the sample with respect to the incident beam direction have two specific effects. It may increase the surface reflection according to the Fresnel equations and the optical depth as $e/cos\theta$ where θ is the tilt and e the thickness. However, the use of such small tilt has a clearly negligible effect on the reflectance measurements because the optical depth and the reflectivity are increased by factors of about 1.007 and 1.00007, respectively compared to the case of normal incidence (i.e. for no tilt).

The hemispherical data are obtained by summing the bidirectional measurements according to Eqs. (32) and (33) with $\Delta\omega_{\theta i}$ the differential solid angle, which subdivides the hemisphere so that:

$$\sum_{i=1}^{36} \Delta\omega_{\theta i} = 4\pi \tag{31}$$

Assuming an azimuthal symmetry, it is possible to obtain the hemispherical measurements as follows:

$$\rho^{\cap} = \sum_{i=1}^{18} \rho"(\theta_i) cos\theta_i \Delta\omega_{\theta i} \tag{32}$$

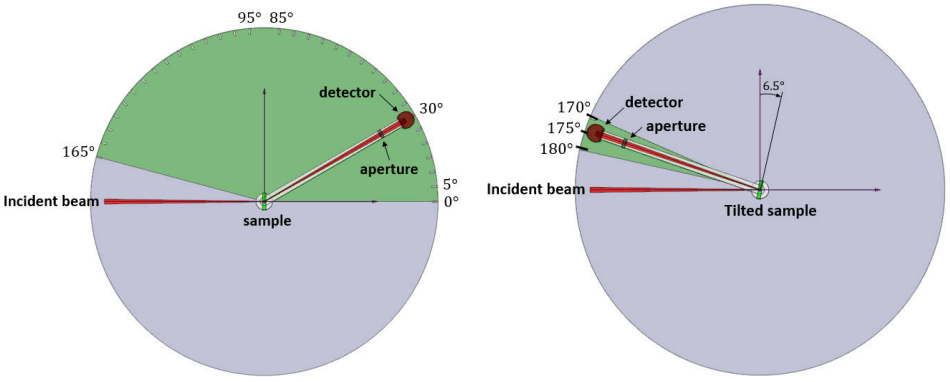

(a) Normal sample

(b) Tilted sample

Figure 6: Distribution of measurement angles.

$$\tau^{\cap} = \sum_{i=1}^{18} \tau"(\theta_i) cos\theta_i \Delta\omega_{\theta i} \tag{33}$$

i is the index of the experimental quadrature and the solid angle $\Delta\omega_{\theta i}$ is calculated with Eqs. (24) and (25). The use of this method rather than using a measurement from an integrating sphere enforces the azimuthal asymmetry of the scattering.

3.3.2. Measurements with samples exhibiting roughness-attenuated and rough boundaries

Before identifying simultaneously the volumetric and surface scattering properties, it was important to verify that the method was able to determine the volumetric properties alone. One way of doing this was to test the inverse method either with a high porosity sample, such as open-cell foams, or a scattering sample exhibiting optically smooth boundaries. The second option was retained here by masking the composite sample boundaries through the use of an index-matching liquid. To do so, the samples were placed one after the other in a liquid having a refractive index similar to the polymer matrix at the wavelength of interest as showed in Figure 7. Two candidate liquids having a refractive index close to those of the resin were tested: the refractive index liquid series A from Cargille Laboratories, with $n = 1.499$ and $n = 1.596$ at a wavelength of 1070 nm. The liquid as well as the container are almost fully transparent at the wavelengths of measurements. The liquid was expected to fill the roughness of the sample surfaces, and consequently, the roughness was expected to disappear due to the index-matching effect. However, it is possible that the smallest roughnesses trap air bubbles so that the roughness of the sample boundaries were not perfectly hidden. This assumption will be discussed again in the result section.

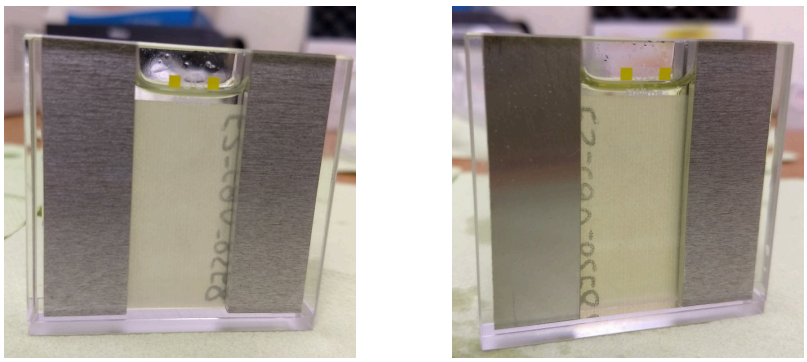

(a) n = 1.499

(b) n = 1.596

Figure 7: Sample in liquid of refractive index n.

In order to determine the most suitable liquid, bidirectional transmittance and reflectance measurements were carried out on a sample made of the container wall and the containers filled with the liquids. The results show that the liquid of refractive index $n = 1.499$ provide the lowest reflectance and highest transmittance close to those of the single container wall. It means that this liquid exhibits very close refractive index as the container wall and permits to minimize the light reflexions at liquid/container interfaces. However the difference with the second liquid ($n = 1.596$) is not significant so that we decided to conduct the experiments considering successively the two liquids.

3.4. Identification method

The objective is to identify three equivalent volumetric parameters, namely the extinction coefficient β_λ, the albedo ω_λ and the asymmetric parameter g_λ and three surface scattering parameters (Cf_{12}, Cf_{21} and σ_G). The identification method is based on the minimization of the sum of the squared residuals:

$$S = \sum_{i=1}^{36} (x_t(i) - x_e(i))^2 + (\tau_t^{\cap} - \tau_e^{\cap})^2 + (\rho_t^{\cap} - \rho_e^{\cap})^2 \tag{34}$$

With $x_t(i)$ the theoretical value of the bidirectional reflectance, $x_t(i) = \rho"(\theta i)$, or transmittance, $x_t(i) = \tau"(\theta i)$, at the measurement angle of index i of the quadrature discretized into 36 angles. $x_e(i)$ is the corresponding experimental values. $\tau_t^{\cap}$ and $\tau_e^{\cap}$ are the theoretical and experimental hemispherical transmittances, respectively, and $\rho_t^{\cap}$ and $\rho_e^{\cap}$ are the theoretical and experimental hemispherical reflectances, respectively.
The Gauss-Newton method is relevant for solving this type of non-linear problem [74]. It has the advantage of converging quickly despite the fact that it may be sensitive to the choice of initial guesses. As in any inverse problem, the number of measurement points must be greater or equal to the number of unknown parameters. We employed here both hemispherical and bidirectional measurements. The greater the number of bidirectional measurements, the more the identification of the phase function is accurate. The Gauss-Newton method is an iterative method enabling to solve the following system:

$$(J^T J)\delta p = J^T r \tag{35}$$

With J the jacobian matrix, i.e. a matrix composed of the first order partial derivatives of the function, calculated through by the MC method. δp the vector of the increments of the unknown parameters and r the vector of the residuals.

$$J = \begin{bmatrix} \frac{\partial \rho^{\cap}}{\partial \beta} & \frac{\partial \rho^{\cap}}{\partial \omega} & \cdots & \frac{\partial \rho^{\cap}}{\partial \sigma_G} \\ \frac{\partial \tau^{\cap}}{\partial \beta} & \frac{\partial \tau^{\cap}}{\partial \omega} & \cdots & \frac{\partial \tau^{\cap}}{\partial \sigma_G} \\ \vdots & \vdots & \ddots & \vdots \\ \frac{\partial \tau"_{36}}{\partial \beta} & \frac{\partial \tau"_{36}}{\partial \omega} & \cdots & \frac{\partial \tau"_{36}}{\partial \sigma_G} \end{bmatrix} ; \delta p = \begin{bmatrix} \delta\beta \\ \delta\omega \\ \delta g \\ \delta C_{fr} \\ \delta C_{ft} \\ \delta\sigma_G \end{bmatrix} ; r = \begin{bmatrix} \rho_{th}^{\cap} - \rho_{exp}^{\cap} \\ \tau_{th}^{\cap} - \tau_{exp}^{\cap} \\ \vdots \\ \tau"_{36,th} - \tau"_{36,exp} \end{bmatrix} \tag{36}$$

As shown in Eqs. (35) and (36), the Gauss-Newton method is based on a calculation of partial derivatives. These derivatives become very sensitive when the residues are small compare to the measurements. The MC method is a stochastic method which is therefore subject to statistical errors. To prevent these errors from disturbing the Gauss-Newton algorithm, the theoretical values are obtained from the average of ten different Monte Carlo runs.

4. Results

4.1. Numerical investigations

The MC simulation and the inverse analysis were implemented in Matlab 7.0.1. The calculation was performed using a working station (Bull R421-E3 Cluster, Intel Xeon Processors E5-2650v2 8C 2.600 GHz 32 Go DDR3, InfiniBand fast network FDR). The MC simulation is a stochastic solution method and its accuracy depends on two factors namely, the number of ray samples, N, and the pseudo-random number generator. By increasing N, the statistical error decreases and the result fluctuation is reduced as shown in Figure 8.

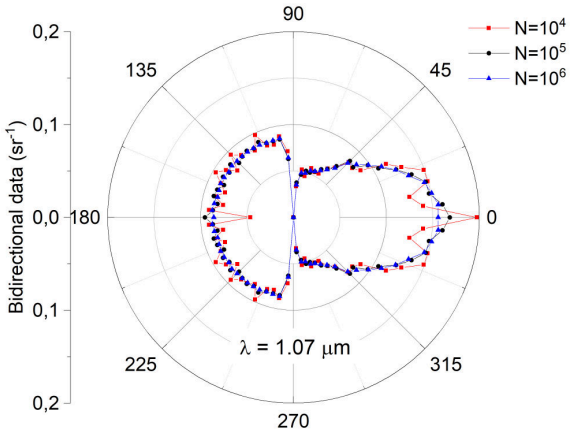

Figure 8: Influence of the number of rays N on the calculated bidirectional transmittance and reflectance.

Nevertheless, the computation time proportionally increases with the number of rays. It is thus important to find a compromise between accuracy and computation time. The maximum standard deviation of the bidirectional transmittances and reflectances as a function of the number of rays is shown in the Figure 9.

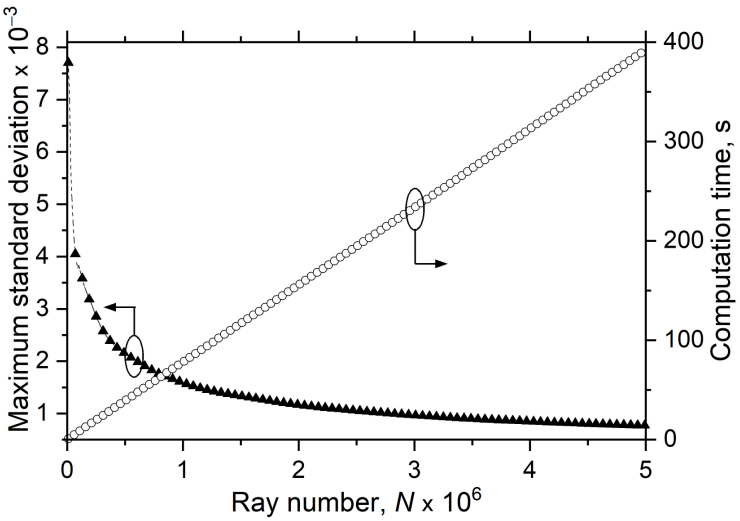

Figure 9: Standard deviation of bidirectional values and time calculation versus the number of rays.

Clearly, the standard deviation decreases while increasing the number of rays and tends towards a limit value. At the same time, the calculation time increases linearly as a function of the ray number. To ensure that the MC simulation error is much smaller than the overall measurement uncertainty, which is estimated to be about 4%, the ray number is fixed to be 10^6. To deal with the error due to the use of a pseudo-random number generator, results are obtained from the average of ten MC runs based on different random seeds.

4.2. Accuracy analysis

In this section, we report the sensitivity analysis of the theoretical model with respect to each unknown parameter and the feasibility of the simultaneous determination of these parameters. To do so, the identified parameters are used as reference data. The study is conducted on the three samples of different thicknesses and focuses on three points: the reduced sensitivity of the model to the parameters, the accuracy of the identification method and the possible correlation between the different parameters.

4.2.1. Sensitivity analysis

The reduced sensitivity matrix contains all the sensitivity coefficients determined for each measurement quantity and is defined as follows:

$$M_{ij} = \frac{\partial x_i}{\partial p_j} * p_j \tag{37}$$

With x_i the bidirectional measurement for i ranging from 1 to 36, and hemispherical transmittance and reflectance for i equal to 37 and 38, respectively. j is one of the six unknown parameters. The sensitivities on hemispherical measurements on the three sample thicknesses are reported in Table 1.

Table 1: Reduced sensitivities on hemispheric measurements.

	β_λ	ω_λ	g_λ	Cf_{12}	Cf_{21}	σ_G
$\rho^\cap$ 16 plies	0.1641	0.8846	0.2662	0.0601	0.0549	0.0619
$\tau^\cap$ 16 plies	0.1711	1.3047	0.3125	0.0268	0.2208	0.0588
$\rho^\cap$ 8 plies	0.0683	0.8178	0.1796	0.0155	0.0178	0.0057
$\tau^\cap$ 8 plies	0.1121	1.1277	0.2126	0.0081	0.1329	0.0026
$\rho^\cap$ 4 plies	0.0427	0.4984	0.09	0.0931	0.026	0.0805
$\tau^\cap$ 4 plies	0.1527	0.8387	0.0551	0.0089	0.2316	0.1174

As expected, the radiative volumetric properties (the extinction coefficient β_λ, the albedo ω_λ and the asymmetry factor g_λ) have a greater sensitivity on hemispherical measurements than the surface properties (the two correction factors Cf_{12} and Cf_{21} and the standard deviation of the Gaussian function σ_G). The behavior of the ray is dependent on the volume properties in all the volume of the sample, while the three surface properties only take place at the surface boundaries. The correction factor Cf_{12}, which is involved in the reflectivity calculation at the irradiated boundary, mainly impacts the reflectance. The correction factor Cf_{21}, which characterizes the future of rays during their interaction with the internal sides of the boundaries, presents a greater sensitivity to the transmittance than to the reflectance. The albedo is the parameter exhibiting the highest sensitivity, which indicates that its identification will be more straightforward. An increasing thickness seems to improve the sensitivity.

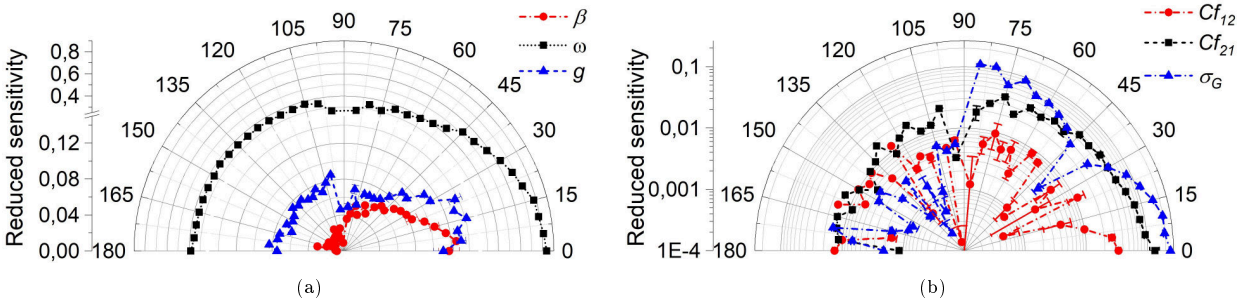

Figure 10: Reduced sensitivities on bidirectional measurements.

The sensitivity analysis of bidirectional data (Figure 10) provides detailed informations about essential measurement angles. Regarding volumetric radiative properties (Figure 10a), the sensitivity of transmittances and reflectances to the albedo ω_λ is about five times higher than those of the extinction coefficient β_λ and the asymmetry parameter g_λ over the entire angular domain. The sensitivities decrease away from the forward direction and then they vary weakly with the angle especially those on reflectances. That means that the forward bidirectional transmittances play a key role in the identification of the volumetric properties while bidirectional reflectances have an equal importance. The determination of the albedo would be definitely relevant due to the high sensitivity of the model. The determination of the extinction coefficient needs some accurate measurements of forward bidirectional transmittances. Finally, the determination of the asymmetry parameter is feasible with both bidirectional transmittances and reflectances. The sensitivities of the model to the surface scattering properties (Figure 10b) are essentially meaningful on bidirectional transmittances.

Surprisingly, the sensitivity of bidirectional data to the correction factor Cf_{12} occurs on the forward transmittances while the sensitivity of hemispherical data to this parameter concerns the reflectance. The use of bidirectional and hemispherical data can clearly help to identify the surface scattering properties.

4.2.2. Confidence interval

In order to evaluate the accuracy of the identified parameters, it is first necessary to estimate the mean standard deviation:

$$\sigma_{moy} = \frac{\sum_{i=1}^{38}(x_{i,exp} - x_{i,theo})^2}{n_{dir} - 1} \tag{38}$$

With $x_{i,exp}$ the experimental value of the hemispherical or the bidirectional data at the angle i and $x_{i,theo}$ the value at the same angle i but obtained with the MC method using as inputs the identified parameters. n_{dir} is the number of measurement points of the quadrature. To measure the uncertainty generated by the identification method a Student's t-test is carried out. The t-test consists in determining a confidence interval of the parameters as a function of Student's distribution and the mean standard deviation of theoretical solutions to experimental data. Student's distribution is a probability law based on the reduced centered normal distribution and the law of χ^2. The matrix P is determined in order to simplify the following calculations.

$$P = \sigma_{moy}[J^t J]^{-1} \tag{39}$$

J being the Jacobian matrix calculated in Eq.(36). The confidence interval δ_{pi} is then obtained as follows:

$$\delta_{pj} = t_\alpha^k \sqrt{P_{j,j}} \tag{40}$$

$P_{j,j}$ refers to the component in the j^{th} column and j^{th} line of the matrix P calculated at Eq. (39). t_α^k is the quantile of order $1-\alpha$ of Student's law at k degrees of freedom. This quantile can be easily obtained based on a Student table. The degree of freedom depends on the number of measurements and the number of parameters studied. It is possible to calculate this degree of freedom by simply subtracting the number of parameters identified from the number of measurements made. In the context of this study, the degree of freedom is therefore 32. The order $1-\alpha$ also called confidence level is arbitrarily set according to the desired precision. In this case, the risk level α is set at 2.5%, the confidence level is therefore 97.5%. The risk level is low in order to ensure the validity of the results without being too restrictive, which would greatly increases the confidence interval. This implies that the studied parameter has a 97.5% chance of being in the confidence interval around the identified value. Then using a Student table, the Student quantile is set to 2.042. As for the sensitivity matrices, this study is conducted on the three samples.

Table 2: Confidence intervals for parameters identified in %.

	4 plies	8 plies	16 plies
β_λ	4.60	1.52	2.57
ω_λ	1.59	0.82	0.60
g_λ	3.69	1.75	1.41
Cf_{12}	3.22	3.62	2.39
Cf_{21}	5.83	4.73	1.77
σ_G	2.08	2.15	1.84

As already highlighted by the sensitivity study, the Student test confirms the thicker the sample is, the more accurate the model is. This behavior essentially concerns the three volumetric radiative properties and this can be explained by the fact that statistically, the thicker a sample is, the more chance there is for a ray to interact with the medium. For the same reason, the sensitivities of each three surface properties are approximately identical regardless of the thickness.

4.2.3. Correlation study

The inverse analysis simultaneously determines six parameters and consequently, it is important to analyze the correlation of these parameters with each other. If one depends on another, the simultaneous identification of these two parameters becomes irrealistic. To quantify the correlation between a parameter i and a parameter j, a correlation coefficient c_{ij} is calculated as follows:

$$c_{ij} = \frac{P_{ij}}{\sqrt{P_{ii}P_{jj}}} \tag{41}$$

with P_{ij} the components of the matrix calculated in Eq. (39). The calculated correction coefficients are reported in Table 3.

Table 3: Correlation coefficients c_{ij} between the identified parameters.

	β_λ	ω_λ	g_λ	Cf_{12}	Cf_{21}	σ_G
β_λ		0.581	0.130	0.852	0.191	0.655
ω_λ	0.581		0.00971	0.566	0.416	0.446
g_λ	0.130	0.00971		0.389	0.136	0.0563
Cf_{12}	0.852	0.566	0.389		0.232	0.405
Cf_{21}	0.191	0.416	0.136	0.232		0.478
σ_G	0.655	0.446	0.0563	0.405	0.478	

These correlation coefficients are calculated for the case of the 16-plies sample, but the results are similar with the other two samples. The values obtained are satisfactory since a correlation coefficient lower than 0.9 indicates that the two parameters are enough decorrelated [74], which is the case here. Consequently, the simultaneous determination of the six parameters is relevant.

4.3. Experimental data

The measurement was carried out on the three glass/epoxy composite samples of different thicknesses, $e = 0.76$, 1.50, and 3.10 mm. The results presented here are obtained at the wavelengths 1070 and 1550 nm, which are the wavelengths of interest for the envisioned application. The values of the bidirectional transmittances and reflectances, reported in Figure 11, are obtained from the spectrometric measurements according to Eq. (29). The black arrow indicates the direction of the incident radiation to the sample. The abscissa represents the polar angle in degrees and the ordinate represents the bidirectional values in sr^{-1}. The data for each sample correspond to the average over ten different measurements. Specifically, for the first five measurements, the installation is unchanged in order to assess the uncertainty of the spectrophotometer. For the other five measurements, the irradiated surface is changed in order to assess the homogeneity of the sample. The average standard deviation of the bidirectional measurements due to the spectrometer uncertainty itself is less than 1% and the one due to the sample non-homogeneity is less than 4% at 1070 nm. However, at the wavelength of 1550 nm, the average standard deviation reaches 10% because of a lower accuracy of the detectors at this wavelength.

The angular reflectance distribution is similar from one sample to another. The bidirectional reflectances are broadly distributed over the reflectance angular domain in the three cases. We explain this trend by the fact that the scattering by the rough irradiated surface dominates the reflectance and such surface scattering is almost isotropic. Concerning the bidirectional transmittances, the transmittance is mainly forward for measurement angles in the range $-40° < \theta < 40°$ otherwise it tends to be isotropic. As expected, the thicker the sample, the lower the transmittance in a given direction is.

In order to reduce the contribution of rough surface scattering to the measured transmittances and reflectances, identical measurements were carried out on the same samples but in this case, they were successively immersed in a rectangular container filled with an index-matching liquid (see Figure 7). Note that the refractive index of the current resin matrix is only approximately known to be between 1.490 and 1.576 according to the supplier's information. For this reason, the measurements were made with two liquids of different refractive indexes as discussed in section 3.2.2. In this manner, one can expect that the bidirectional transmittance and reflectance measurements out of the forward and the backward solid angles are mainly due to volume scattering within the material. Focusing on the wavelength of 1070 nm, the Figure 12 show that

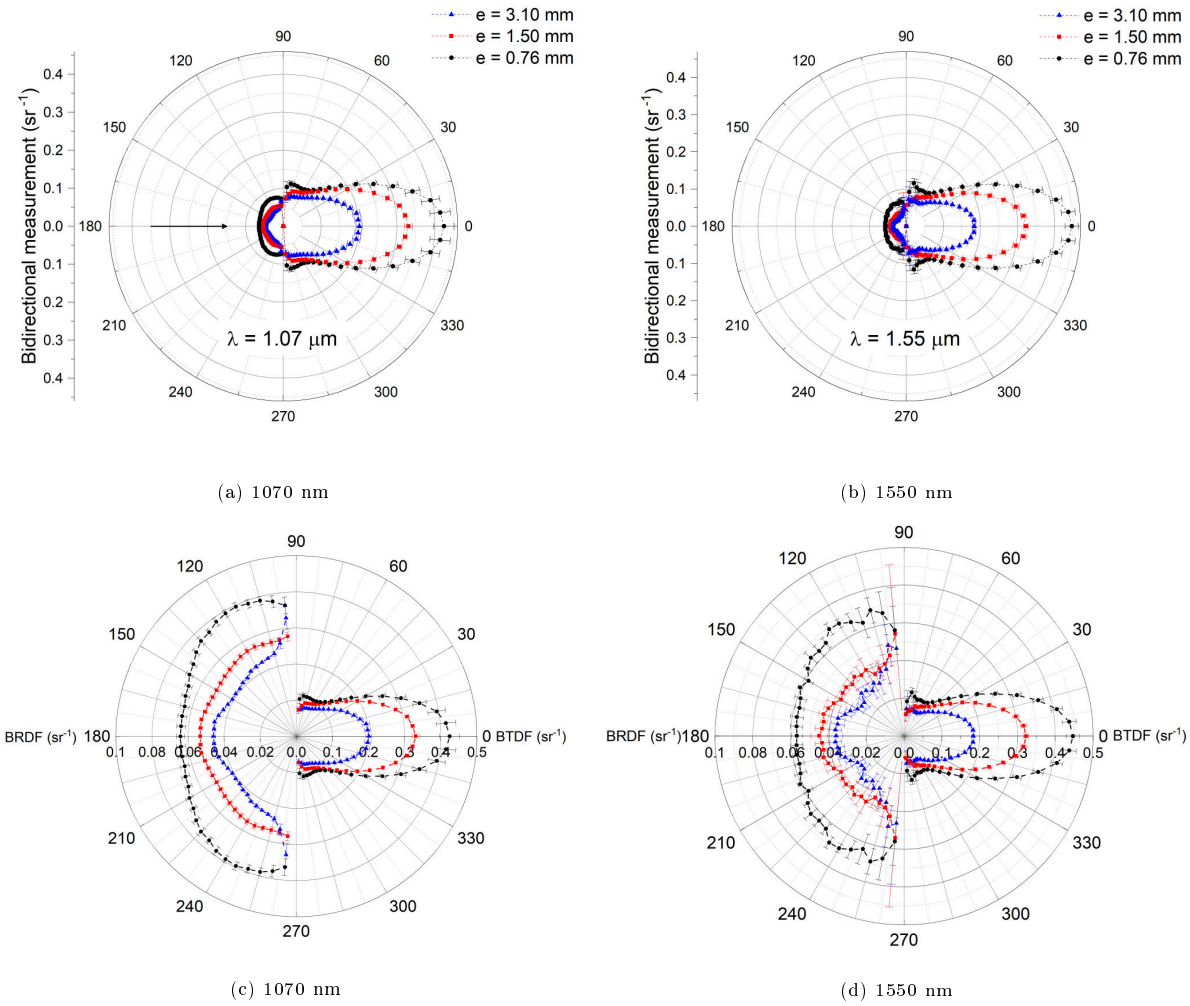

(a) 1070 nm

(b) 1550 nm

(c) 1070 nm

(d) 1550 nm

Figure 11: Experimental bidirectional transmittance and reflectance data of the three investigated samples with error bars at 1070 nm (a) and 1550 nm (b). Same figures with a different scale for the Bidirectional Reflectance Distribution Function (BRDF) and the Bidirectional Transmittance Distribution Function (BTDF) at 1070 nm (c) and 1550 nm (d).

the angular distribution of the bidirectional transmittance and reflectance measurements in the presence of an index-matching liquid differ significantly from those obtained with a non-immersed sample. The transmittance lobe is more pronounced in the forward direction whereas the reflectance lobe is still quasi-isotropic, except that a peak appears in the backward direction. The reflectance peaks come clearly from the specular reflection at the glass container wall. More interestingly, the contribution of scattering at sample boundaries is definitely decreased and that explains the significant change on the angular distribution of transmittances especially for thin samples. However, this comparison does not enable us to confirm that the rough boundary scattering is completely canceled by the use of an index-matching liquid.

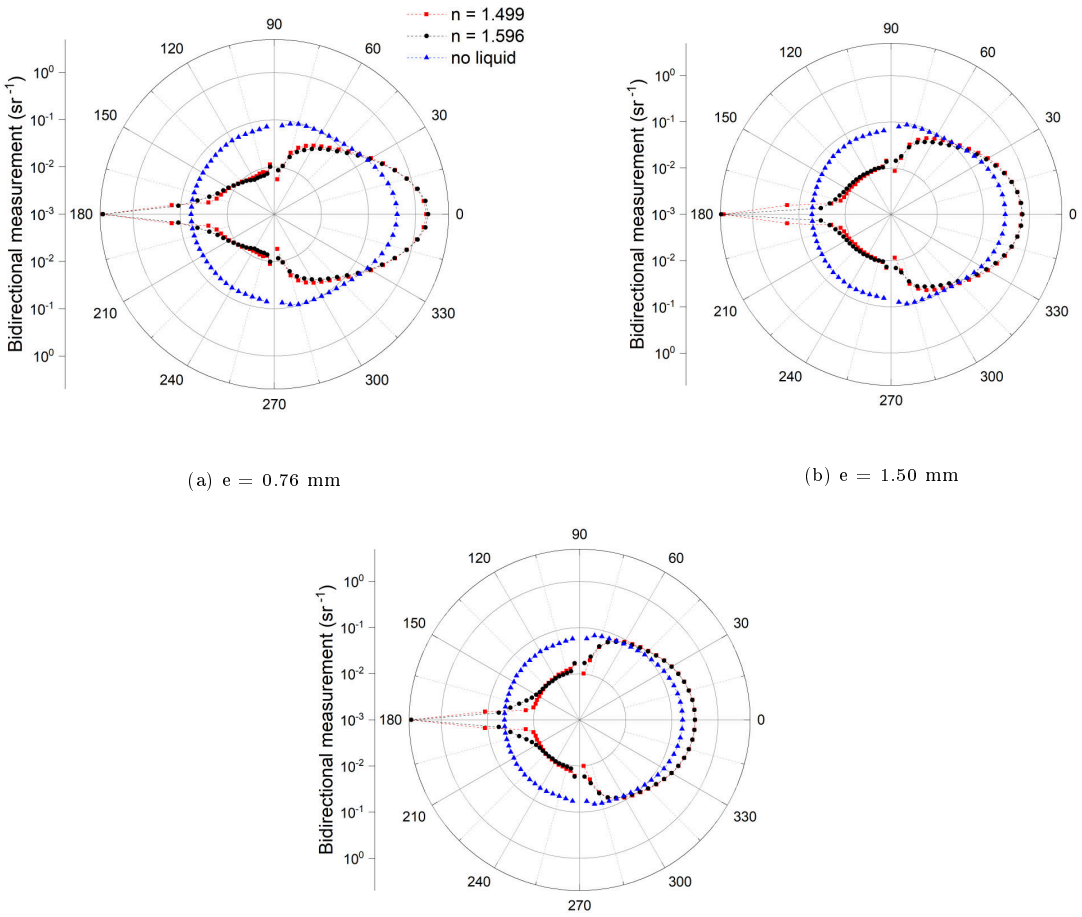

(a) e = 0.76 mm

(b) e = 1.50 mm

(c) e = 3.10 mm

Figure 12: Experimental bidirectional values in log scale for the sample alone and the sample immersed at 1070 nm

The hemispherical data are obtained from Eqs. (32) and (33) by using the bidirectional measurements reported in Figure 12. The contribution of surface scattering to the bidirectional transmittances and reflectances of the sample is significant as it can be noticed in Figure 12. Tables 4 and 5 compare the measured hemispherical transmittances and reflectances between the sample alone and the same sample immersed in the container with the liquid of refractive index of $n = 1.499$ or $n = 1.596$ for the wavelength of 1070 nm.

Table 4: Experimental hemispherical reflectance at 1070 nm.

	sample alone	$n = 1.499$	$n = 1.596$
e = 0.76 mm	0.189	0.0756	0.0785
e = 1.50 mm	0.183	0.0777	0.0816
e = 3.10 mm	0.152	0.0776	0.0818

Table 5: Experimental hemispherical transmittance at 1070 nm.

	sample alone	$n = 1.499$	$n = 1.596$
e = 0.76 mm	0.500	0.688	0.675
e = 1.50 mm	0.454	0.604	0.563
e = 3.10 mm	0.335	0.474	0.466

We can observe that the liquid of the refractive index of 1.499 exhibits the smallest hemispherical reflectance and largest transmittance for the same thickness. This enables us to conclude that the resin refractive index at

1070 nm is near the value of 1.5. The presence of rough boundaries increases the reflectance and consequently decreases the transmittance. It is therefore very important to take the presence of the surface roughness into account when characterizing radiative transfer through composite samples.

4.4. Identification of the radiative properties

Analyzing the angular distribution of the bidirectional transmittances and reflectances gives an idea of the surface scattering probability distribution function $p(\mu)$ to be used in the surface reflectivity model, Eq. (11). The quasi-isotropic behavior of the bidirectional reflectance can be represented by a cosine distribution function, Eq. (12). The angular distribution of the bidirectional transmittance lobe can be represented by the average of a Gaussian function, Eq. (13), whose standard deviation is calculated during identification, and a cosine function, Eq. (12). Note that other combinations of these distribution functions were tested but these choices provide the best measurement predictions.
The Gauss-Newton-based inverse method is employed to identify the six unknown parameters. When the residues, given by Eq. (34), are lower than the experimental standard deviation, i.e. 4%, we consider that the inverse analysis is sufficiently accurate enough to be aborted. The six radiative properties obtained by the identification at 1070 nm and at 1550nm, for each sample thickness without any index-matching liquid are reported in Table 6.

Table 6: Radiative parameters identified at 1070 nm (a) and at 1550 nm (b).

	e = 3.10 mm	e = 1.50 mm	e = 0.76 mm
β_λ [m^{-1}]	762 ± 35	966 ± 16	1063 ± 29
ω_λ	0.896 ± 0.007	0.884 ± 0.006	0.901 ± 0.003
g_λ	0.858 ± 0.010	0.885 ± 0.010	0.908 ± 0.012
Cf_{12}	0.505 ± 0.025	0.520 ± 0.005	0.648 ± 0.072
Cf_{21}	0.688 ± 0.020	0.577 ± 0.016	0.681 ± 0.054
σ_G	0.483 ± 0.005	0.411 ± 0.007	0.384 ± 0.013

(a) 1070 nm

	e = 3.10 mm	e = 1.50 mm	e = 0.76 mm
β_λ [m^{-1}]	807 ± 49	1027 ± 70	1170 ± 69
ω_λ	0.854 ± 0.014	0.846 ± 0.010	0.883 ± 0.011
g_λ	0.940 ± 0.016	0.951 ± 0.010	0.936 ± 0.005
Cf_{12}	0.623 ± 0.085	0.566 ± 0.045	0.560 ± 0.047
Cf_{21}	0.720 ± 0.038	0.598 ± 0.059	0.611 ± 0.051
σ_G	0.463 ± 0.010	0.385 ± 0.009	0.362 ± 0.005

(b) 1550 nm

The albedo ω_λ and the asymmetry factor g_λ vary little from one sample to another. These two properties only depend on the scatterers, which are the glass fibers in this case. As the size, the shape and the orientation of the fibers strands are identical for the three samples, it is expected to retrieve close values of the albedo ω_λ and the asymmetry factor g_λ between the three samples. Surprisingly, the extinction coefficient β_λ decreases when increasing the thickness. This trend tends to indicate that the manufacturing process of composites modifies the internal structure of the samples such as its compactness. The parameters Cf_{12} and Cf_{21} characterize the strength of the rough surface scattering while σ_G defines the width of the Gaussian distribution function, which seems to be narrower for the thinner samples. The values of the coefficient Cf_{12} or Cf_{21} are approximately identical for the three samples. However, the parameter Cf_{12} is systematically smaller than the parameter Cf_{21}. This is explained by the fact that the overall reflection of radiation from the air to the sample, i.e. with the parameter Cf_{12}, is weaker than the overall reflection of radiation from the sample to the air, i.e. with the parameter Cf_{21}, because of the existence of total reflection of radiation beams at certain angles.

In order to assess the pertinence of our approach, the identification process was also carried out with measurements for samples immersed within the index-matching liquids as explained in part 3.3.2. In this case the samples are considered smooth and the surface scattering is assumed to be negligible. Only the three volumetric properties are identified here. The extinction coefficient β_λ, the albedo ω_λ and the asymmetry factor g_λ identified for the samples with smooth surfaces are reported in Tables 7 and 8 for the wavelength of 1070 nm. The difference between the results we obtained with the sample alone (rough surface) and with the sample immersed in an index-matching liquid (smooth surface) is also given in these tables.

Table 7: Parameters identified with the sample in the liquid $n = 1.499$ at 1070 nm.

	e = 3.10 mm	difference	e = 1.50 mm	difference	e = 0.76 mm	difference
β_λ $[m^{-1}]$	797.7	4.8%	1015.1	0.6%	1293.7	6.5%
ω_λ	0.836	6.2%	0.826	6.7%	0.809	5.9%
g_λ	0.910	7.8%	0.890	5.4%	0.839	1.6%

Table 8: Parameters identified with the sample in the liquid $n = 1.596$ at 1070 nm.

	e = 3.10 mm	difference	e = 1.50 mm	difference	e = 0.76 mm	difference
β_λ $[m^{-1}]$	837.2	0.1%	1040.2	3.1%	1319.8	8.7%
ω_λ	0.862	3.4%	0.861	2.7%	0.811	5.7%
g_λ	0.884	4.8%	0.810	4.1%	0.840	1.5%

The values of the volumetric radiative properties of non-immersed samples differ on average by 5% with the liquid of refractive index $n = 1.499$ and by 3.8% for the liquid of refractive index $n = 1.596$. These differences are comparable to the measurement error about 4%. Therefore, the retrieved volumetric radiative properties with the rough sample are physically consistent and this enable to validate the surface diffusion model.

It is now possible to compare the bidirectional measurements and the bidirectional data returned by the Monte Carlo simulation from the six identified parameters to judge their relevance and the validity of the method. The results are given for the wavelength of 1070 nm in Figure 13 and in Table 9, respectively.

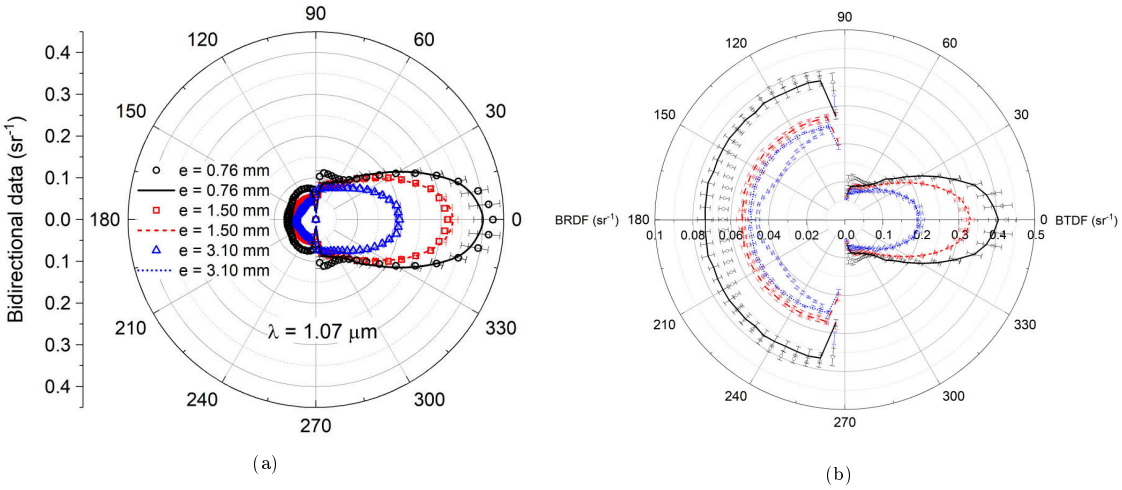

(a) (b)

Figure 13: Experimental and theoretical bidirectional data of the three samples at 1070 nm. Symbols:Measurements, Curves:MC calculation (a) and the same figure with a different scale for the BRDF and the BTDF part (b).

Table 9: Theoretical hemispherical reflectance and transmittance and their deviation (in %) with respect to measurements at 1070 nm.

	$\rho^\cap$	diff	$\tau^\cap$	diff
e = 0.76 mm	0.2016	6.66%	0.4918	1.52%
e = 1.5 mm	0.1825	0.491%	0.4562	0.485%
e = 3.1 mm	0.1524	0.727%	0.3377	0.896%

The bidirectional and hemispherical transmittances and reflectances computed with the MC method are very close to the experimental values. Interestingly, the difference is even less than the measurements error. The good match between theoretical and experimental reflectances and transmittances proves the relevance of the proposed approach to determine the radiative properties of semi-transparent rough composite samples.

5. Conclusion

The radiative transfer in semi-transparent composite media with rough boundaries is modelled by the RTE along with six unknown parameters, which include three volumetric and three surface scattering properties. The Gauss-Newton identification method is employed to determine six unknown parameters. The method is based on a minimization of the sum of the squared residues between the experimental and theoretical values of the bidirectional and hemispherical transmittances and reflectances. The theoretical values are obtained by resolution of the RTE via the Monte Carlo method with a Henyey and Greenstein phase function. Boundaries are treated as semi-transparent and scattering. A spectrophotometric device equipped with a goniometer enables to measure bidirectional transmittances and reflectances on 36 different discrete directions of scattering distributed uniformly over a horizontal plane around the sample. The identifications were carried out on samples of fiberglass/epoxy composite material of three different thicknesses with rough interfaces and the same samples immersed in index-matching liquids. The similarity of the results from the two manners of samples conditioning leads to the conclusion that the volumetric radiative properties of a woven reinforced composite material having rough scattering boundaries can be well determined from the proposed inverse analysis of parameter identification.

The method could be further improved by adding a more realistic phase function such as a phase function using a series of Legendre polynomials. Subsequently, this method could be incorporated into a coupled heat transfer model in order to more precisely characterize the radiative exchanges, heat transfer and possible material damage in the presence of high flux laser irradiation.

Acknowledgements

The authors are grateful to Dr J. Adrien and Dr. E. Maire from the laboratory of "Matériaux : Ingénierie et Science (MATEIS UMR 5510 CNRS - INSA Lyon - Université de Lyon 1)" for performing the X-ray tomography imaging of composite samples. The authors gratefully acknowledge the DGA for the additional funding.

Appendix

A.1 Validation of the experimental method

A.1.1. Validation of the experimental method for smooth boundaries

In order to validate the experimental setup, measurements were carried out on a smooth glass sample of 3 mm thickness (ref. B270® i Ultra-White Glass from Schott company) whose real part of the complex refractive index is known (see table A.1). The exact values of transmittance and reflectance can be obtained, by calculation from the EM wave theory according to [38]:

$$\rho"(\theta) = R_{12}(\theta) + \frac{R_{21}(\theta)(1-R_{12}(\theta))^2 e^{-2ke}}{1-R_{12}(\theta)R_{21}(\theta)e^{-2ke}}, \quad \theta = \pi \tag{42}$$

$$\tau"(\theta) = \frac{(1-R_{12}(\theta))(1-R_{21}(\theta))e^{-2ke}}{1-R_{12}(\theta)R_{21}(\theta)e^{-2ke}}, \quad \theta = 0 \tag{43}$$

with $R_{ij}(\theta)$ the reflectivity for a smooth surface calculated with Fresnel equations, k the imaginary part of the complex refraction index and e the thickness of the sample. The transmittance and reflectance data of the sample are obtained from the bidirectional measurements, Eq. (29) for an beam normally incident on the sample surface. The results including experimental uncertainties are compiled in the table below.

Table A.1: Reflectance and transmittance for an beam normally incident on the sample obtained by calculation (calc) and from the bidirectional setup (bidi) at different wavelength.

	n	k	$\tau"(\theta)_{calc}$	$\tau"(\theta)_{bidi}$	$\rho"(\theta)_{calc}$	$\rho"(\theta)_{bidi}$
$\lambda = 2000$ nm	1.4990	0	92.23	92.48 ± 1.31	8.09	8.41 ± 0.63
$\lambda = 1700$ nm	1.5035	0	92.16	92.67 ± 1.17	8.17	8.55 ± 0.73
$\lambda = 1400$ nm	1.5075	0	92.09	92.66 ± 1.61	8.25	8.47 ± 0.90
$\lambda = 1100$ nm	1.5115	0	91.99	91.90 ± 1.08	8.35	8.59 ± 0.36
$\lambda = 800$ nm	1.5164	0	91.92	91.69 ± 0.60	8.43	8.35 ± 0.37

The measurements and calculation give equivalent results. However, it should be noted that as the wavelength increases, the calculation method loses precision as the glass begins to absorb partially radiation, from around 1600 nm, while in our calculation the absorption index k is fixed to be equal to zero due to lack of accurate data. The small differences observed fall entirely within the experimental errors.

A.1.1. Validation of the experimental method for rough boundaries

In order to assess the validity of bidirectional measurements and also to evaluate the suitability of the azimuthal asymmetry hypothesis, the hemispherical measurements obtained with an integrating sphere (sphere of a diameter of 150 mm with an operational wavelength range from 400 to 2500 nm, equipped with a PMT and a TE Cooled PbS detector) and the hemispherical data obtained from bidirectional measurements through Eqs. (32) and (33) were analysed. These measurements are obtained from the same spectrophotometer described in 3.3.1, and they differ only by the signal acquisition devices (i.e. integrating sphere versus goniometry system). The comparison is reported in the following table.

Table A.2: Hemispherical reflectance and transmittance obtained with the integrating sphere $\rho^{\cap}_{sphere}$,$\tau^{\cap}_{sphere}$ and from the bidirectional measurements $\rho^{\cap}_{bidi}$,$\tau^{\cap}_{bidi}$ at 1070 nm.

	$\rho^{\cap}_{sphere}$	$\rho^{\cap}_{bidi}$	diff	$\tau^{\cap}_{sphere}$	$\tau^{\cap}_{bidi}$	diff
e = 0.76 mm	0.2370	0.2016	14.93%	0.521	0.4918	5.60%
e = 1.50 mm	0.1871	0.1825	2.46%	0.467	0.4562	2.31%
e = 3.10 mm	0.1499	0.1524	1.64%	0.341	0.3377	0.96%

The hemispherical reflectances and transmittances retrieved from bidirectional measurements along with azimuthal symmetry hypothesis agree globally well with those from direct measurements with the integrating sphere. The discrepancy is only significant for the thin sample and more especially on hemispherical reflectance data.

A.1.3. Study of the azimuthal symmetry hypothesis

Figure A.1 reports the bidirectional transmittances and reflectances obtained for different rotation angles of the sample with respect to the incident light direction. The effect of the sample orientation with respect to the incident light direction is only meaningful for the thin sample (0.76 mm thickness). It is known that the scattering by a single fiber or a cylinder is orientation dependent. For the thin sample, the incident radiation undergoes few scattering before crossing the sample and this explains the orientation dependent properties of fibers composing the sample. Inversely, for thick samples, multiple scattering by the presence of various plies takes place and tends to smooth out the fiber orientation effect.

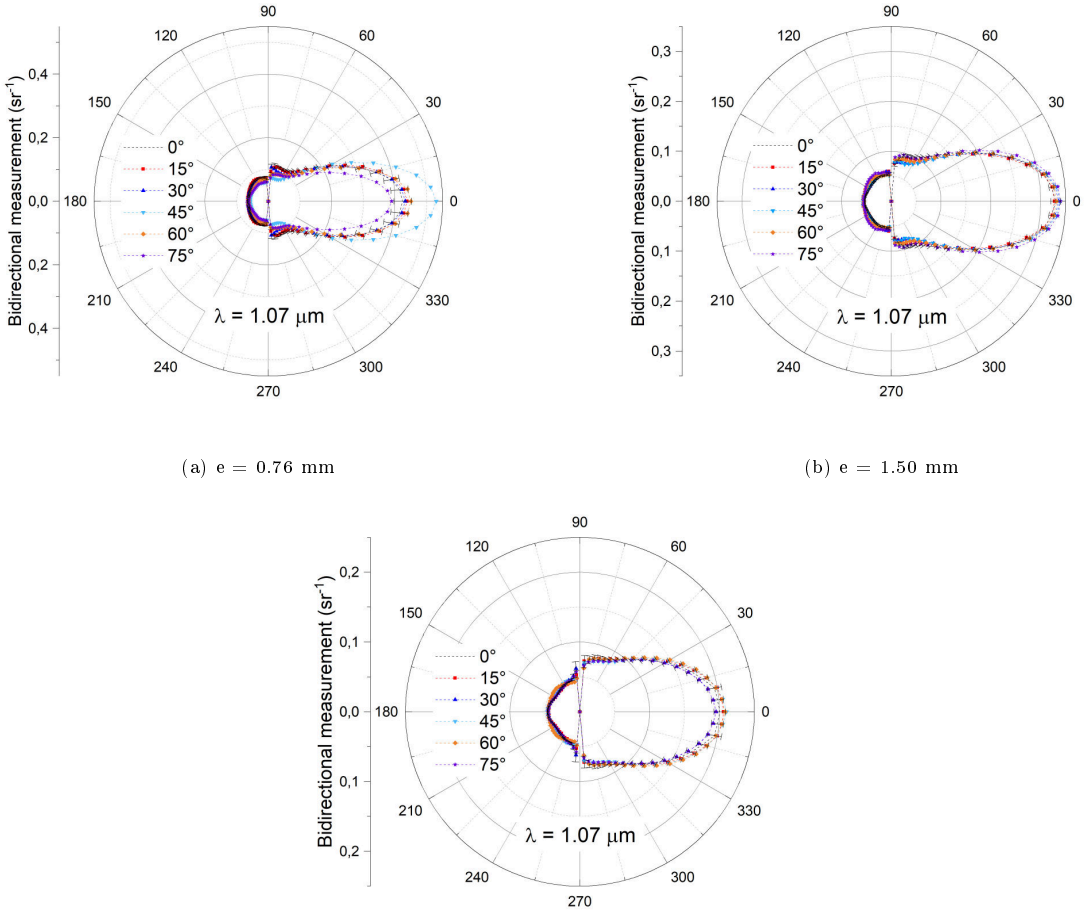

(a) e = 0.76 mm

(b) e = 1.50 mm

(c) e = 3.10 mm

Figure A.1: Bidirectional measurements at 1070 nm at different angles of inclination of the three samples of thicknesses (a) 0.76 mm, (b) 1.50 mm, and (c) 3.10 mm.

This analysis points out the limit of the azimuthal symmetry assumption in the case of thin woven reinforced composite materials. In such a case, the inverse analysis could be conducted on samples of different inclinations with respect to the incident light direction.

A.2 Verification of the implemented Monte Carlo simulation

To assess the accuracy of the current MC method, we conducted a comparative study against the well-established DOM using a high order Gaussian quadrature schema with 60 points [24].We considered the case of absorbing and scattering plane parallel slabs exhibiting non-participating (i.e. transparent) or Fresnel (i.e. optically smooth) boundaries for which the accuracy of DOM has been widely proven. For simplicity reason, the samples with optically smooth boundaries are characterized by a refractive index $n = 1.5$ and surrounded by a vacuum.

Table A.3 summarizes the hemispherical results for media having different couples of radiative properties (optical thickness, τ, scattering albedo, ω, and asymmetry parameter, g) relevant to composite samples but with non-participating boundaries (i.e. $R_{12}(\mu) = R_{21}(\mu) = 0$ for any value of μ in Eq. (11)). Table A.4 shows the results for the same semitransparent media but with Fresnel boundaries (i.e. $Cf_{12} = Cf_{21} = 1$ and $p(\mu) = 1$ for $\mu = \mu'$ and 0 otherwise in Eq. (11)). Clearly, the two computation methods show very good agreement for both types of boundaries. The comparison of the MC bidirectional data to the reference results, depicted in figure A.3, is also very satisfying. These comparisons allow to confirm the suitability of the implemented MC simulation especially for samples with transparent or Fresnel boundaries.

Table A.3: Hemispherical reflectance and transmittance calculated with the MC method and the DOM for different parameters with $n = 1$ and the difference between the two methods.

	case 1 $\omega = 0.5, g = 0$		case 2 $\omega = 0.5, g = 0.9$		case 3 $\omega = 0.9, g = 0$		case 4 $\omega = 0.9, g = 0.9$	
	$\rho^{\cap}$	$\tau^{\cap}$	$\rho^{\cap}$	$\tau^{\cap}$	$\rho^{\cap}$	$\tau^{\cap}$	$\rho^{\cap}$	$\tau^{\cap}$
$\tau = 0.15$ MC	0.0306	0.8919	0.0014	0.9253	0.0613	0.9215	0.0029	0.9819
$\tau = 0.15$ DOM	0.0311	0.8915	0.0014	0.9257	0.0613	0.9215	0.0029	0.9819
difference [%]	1.61	0.04	0	0.04	0.16	0	0	0
$\tau = 1$ MC	0.0997	0.4448	0.0050	0.5894	0.2683	0.5894	0.0184	0.8775
$\tau = 1$ DOM	0.0995	0.4445	0.0050	0.5895	0.2687	0.5900	0.0181	0.8779
difference [%]	0.20	0.07	0	0.02	0.15	0.10	1.66	0.05

Table A.4: Hemispherical reflectance and transmittance calculated with the MC and the DOM method for different parameters with $n = 1.5$ and the difference between the two methods.

	case 1 $\omega = 0.5, g = 0$		case 2 $\omega = 0.5, g = 0.9$		case 3 $\omega = 0.9, g = 0$		case 4 $\omega = 0.9, g = 0.9$	
	$\rho^{\cap}$	$\tau^{\cap}$	$\rho^{\cap}$	$\tau^{\cap}$	$\rho^{\cap}$	$\tau^{\cap}$	$\rho^{\cap}$	$\tau^{\cap}$
$\tau = 0.15$ MC	0.0786	0.8086	0.0710	0.8509	0.1129	0.8418	0.0769	0.9006
$\tau = 0.15$ DOM	0.0812	0.8071	0.0720	0.8492	0.1144	0.8403	0.0774	0.9000
difference [%]	3.20	0.18	1.39	0.20	1.31	0.18	0.65	0.07
$\tau = 1$ MC	0.0838	0.3734	0.0527	0.5282	0.2212	0.5052	0.0818	0.7679
$\tau = 1$ DOM	0.0846	0.3736	0.0545	0.5273	0.2218	0.5050	0.0845	0.7660
difference [%]	0.95	0.05	3.30	0.17	0.27	0.04	3.20	0.25

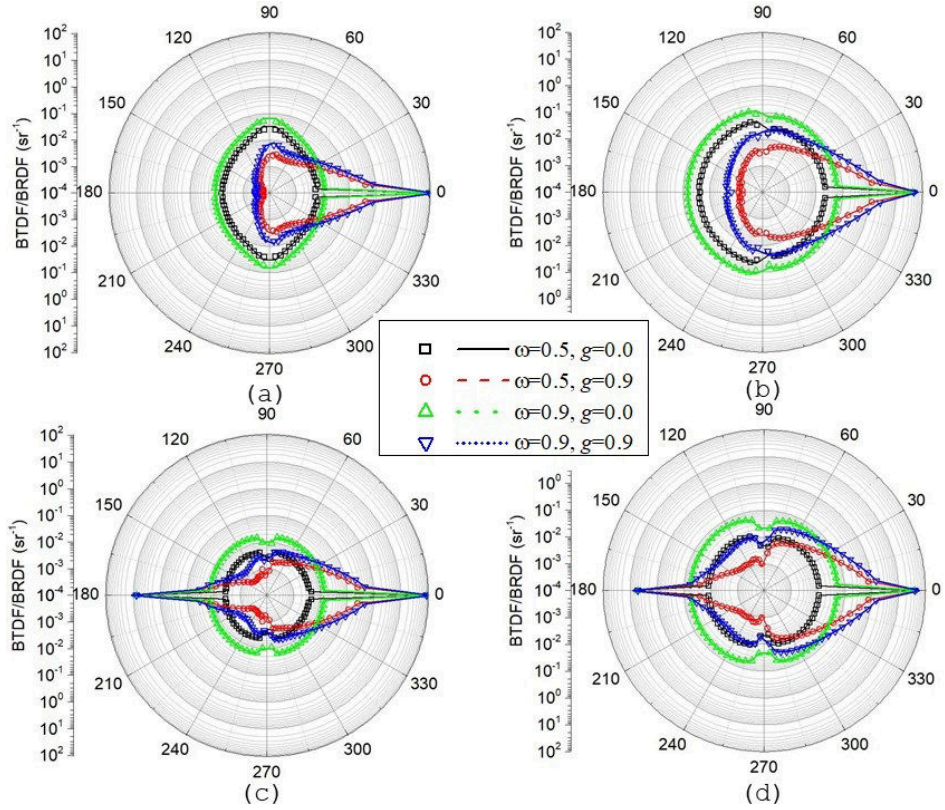

Figure A.2: Bidirectional reflectances and transmittances computed from MC simulation (symbols) and DOM (curves) for media with transparent (a and b) and Fresnel boundaries (c and d). n=1 and τ=0.15 (a); n=1 and τ=1 (b); n=1.5 and τ=0.15 (c); and n=1.5 and τ=1 (d).

To assess the suitability of the MC method for samples with rough boundaries, we analyze the influence of each boundary scattering parameter, especially Cf_{ij} and σ_G involved in Eqs. (11) and (13), on the bidirectional reflectance and transmittance. The parameter values of interest fall in the range $0.5 \leq Cf_{12} = Cf_{21} \leq 1$ and $0 \leq \sigma_G \leq 0.3$). Note that the combination $Cf_{12} = Cf_{21} = 1$ and $\sigma_G = 0$ allow to retrieve the results of optically smooth boundaries. The figure A.4 shows the bidirectional data corresponding to different couples of scattering parameters. In all cases, the sample are characterized by the following radiative properties, which are relevant to the investigated composite materials: $\tau = 1$, $\omega = 0.9, g = 0.9, n = 1.5$. As expected, the case with the boundary scattering properties ($Cf_{ij} = 0.9$ and $\sigma_G = 0.1$) exhibits a behaviour similar to that of smooth boundaries ($Cf_{ij} = 1$ and $\sigma_G = 0$). The main difference occurs around the peaks of forward and backward directions where the parameters $Cf_{ij} = 0.9$ and $\sigma_G = 0.1$ lower and broader these peaks and lead to forward and backward scattering lobes. Increasing the σ_G (e.g. from 0.1 to 0.3) broadens significantly the forward and backward scattering lobes. On the other hand, decreasing Cf_{ij} (typically from 0.9 to 0.5) similarly enhances the scattering out of the forward and backward scattering lobes. It can be seen clearly that the boundary scattering parameters affect differently the bidirectional response of the sample while they enable to retrieve the limiting response of optically smooth slabs. This additional study tends to demonstrate the ability of the Monte Carlo simulation to dissociate quantitatively the contribution of boundary scattering from the overall bidirectional response of rough samples.

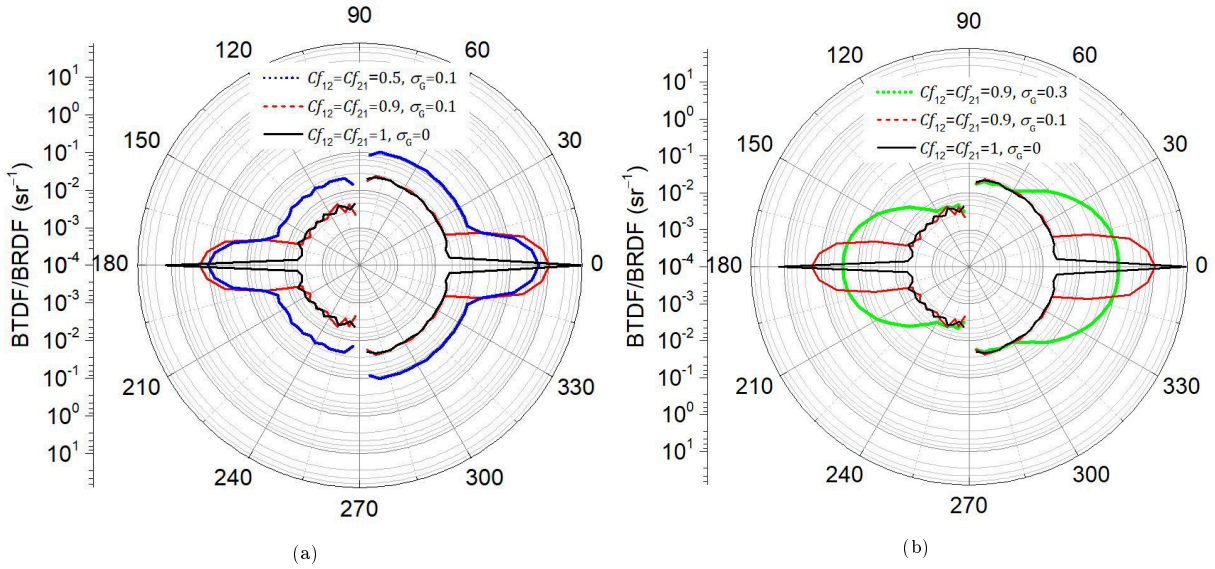

(a) (b)

Figure A.3: BRDF and BTDF of semi-transparent samples ($\tau = 1$, $\omega = 0.9, g = 0.9, n = 1.5$) having different boundary scattering properties.

References

[1] L. Dombrovsky, J. Randrianalisoa, W. Lipinski, D. Baillis, Approximate analytical solution to normal emittance of semi-transparent layer of an absorbing, scattering, and refracting medium, Journal of Quantitative Spectroscopy & Radiative Transfer 112 (2011) 1987–1994.

[2] R. Coquard, D. Baillis, J. Randrianalisoa, Homogenous phase and multi-phase approches for modeling transfer in foams, International Journal of Thermal Sciences 50 (2011) 1648–1663.

[3] P. Boulet, G. Jeandel, G. Morlot, Model of radiative transfer in fibrous media - matrix method, International Journal of Heat and Mass Transfer 30 (18) (1993) 4287–4297.

[4] V. Allheily, L. Merlat, G. L'Hostis, Experimental and numerical investigations of laser-induced thermal effects on composite materials, Proc. SPIE 11162, High Power Lasers: Technology and Systems, Platforms, Effects III, 111620P (2019).

[5] S. Zhao, al., Influence of Scattering Phase Function on Estimated Thermal Properties of Al2o3 Ceramic Foams, International Journal of Thermophysics 40 (11) (2019).

[6] G. Barreto, P. Canhoto, M. Collares-Pereira, Combined experimental and numerical determination of the asymmetry factor of scattering phase functions in porous volumetric solar receivers, Solar Energy Materials and Solar Cells 206 (2020).

[7] J. Petrasch, P. Wyss, A. Steinfeld, Tomography-based Monte Carlo determination of radiative properties of reticulate porous ceramics, Journal of Quantitative Spectroscopy & Radiative Transfer 105 (2) (2007) 180–197.

[8] Y. Li, X.-L. Xia, C. Sun, S.-D. Zhang, H.-P. Tan, Volumetric radiative properties of irregular open-cell foams made from semitransparent absorbing-scattering media, Journal of Quantitative Spectroscopy & Radiative Transfer 224 (2019) 325–342.

[9] P. Parthasarathy, P. Habisreuther, N. Zarzalis, Identification of radiative properties of reticulated ceramic porous inert media using ray tracing technique, Journal of Quantitative Spectroscopy & Radiative Transfer 113 (15) (2012) 1961–1969.

[10] S. Le Foll, A. Delmas, F. André, Identification of radiative properties for heterogeneous materials at high temperature, International Journal of Thermal Sciences 120 (2017) 314–320.

[11] Y. Dauvois, D. Rochais, F. Enguehard, J. Taine, Statistical radiative modeling of a porous medium with semi transparent and transparent phases : Application to a felt of overlapping fibres, International Journal of Heat and Mass Transfer 106 (2016) 601–618.

[12] G. Jeandel, P. Boulet, G. Morlot, Radiative transfer through a medium of silica fibres oriented in parallel planes, International Journal of Heat and Mass Transfer 36 (2) (1993) 531–536.

[13] R. Coquard, D. Baillis, Radiative properties of dense fibrous containing fibres in the geometric limit, Journal of Heat Transfer 128 (10) (2016) 1022–1030.

[14] J. Marschall, F. Milos, The calculation of anisotropic extinction coefficients for radiation diffusion in rigid fibrous ceramic insulations, International Journal of Heat and Mass Transfer 40 (3) (1997) 627–634.

[15] K. Y. Wang, C. L. Tien, Radiative heat transfer through opacified fibers and powders, Journal of Quantitative Spectroscopy & Radiative Transfer 30 (3) (1983) 213–223.

[16] K. Y. Wang, S. Kumar, C. L. Tien, Radiative transfer in thermal insulations of hollow and coated fibers, Journal of Thermophysics and Heat Transfer 1 (4) (1987) 289–300.

[17] C. L. Lee, Radiative Transfer through a Fibrous Medium : Allowance for Fiber Orientation, Journal of Quantitative Spectroscopy & Radiative Transfer 36 (3) (1986) 253–263.

[18] C. L. Lee, Scattering Phase Function for Fibrous Media, International Journal of Heat and Mass Transfer 33 (10) (1990) 2183–2190.

[19] T. W. Tong, C. L. Tien, Radiative Heat Transfer in Fibrous Insulations—Part I: Analytical Study, Journal of Heat Transfer 105 (1) (1983) 70–75.

[20] T. W. Tong, Q. S. Yang, C. L. Tien, Radiative Heat Transfer in Fibrous Insulations—Part II: Experimental Study, Journal of Heat Transfer 105 (1) (1983) 76–81.

[21] A. Milandri, F. Asllanaj, G. Jeandel, Determination of radiative properties of fibrous media by an inverse method - comparison with the Mie theory, Journal of Quantitative Spectroscopy & Radiative Transfer 74 (5) (2002) 637–653.

[22] H. K. Tagne, D. Baillis, Radiative Heat Transfer Using Isotropic Scaling Approximation: Application to Fibrous Medium, Journal of Heat Transfer 127 (10) 1115–1123.

[23] Y. Zhao, G. H. Tang, M. Du, Numerical study of radiative properties of nanoporous silica aerogel, International Journal of Thermal Sciences 89 (2015) 110–120.

[24] J. Randrianalisoa, D. Baillis, L. Pilon, Improved Inverse Method for Radiative Characteristics of Closed-Cell Absorbing Porous Media, Journal of Thermophysics and Heat Transfer 20 (4) (2006) 871–880.

[25] O. Rozenbaum, D. De Sousa Meneses, P. Echegut, Texture and Porosity Effects on the Thermal Radiative Behavior of Alumina Ceramics, International Journal of Thermophysics 30 (2009) 580–590.

[26] W. Lipinski, D. Keene, S. Haussener, J. Petrasch, Continuum radiative heat transfer modeling in geometrical optics, Journal of Quantitative Spectroscopy & Radiative Transfer 111 (2010) 2474–2480.

[27] L. Dombrovsky, J. Randrianalisoa, D. Baillis, Infrared radiative properties of polymer coatings containing hollow microspheres, International Journal of Heat and Mass Transfer 50 (2007) 1516–1527.

[28] S. Rudisill, L. Venstrom, N. Petkovich, T. Quan, N. Hein, D. Boman, J. Davidson, A. Stein, Enhanced Oxidation Kinetics in Thermochemical Cycling of CeO2 through Templated Porosity, Journal of Physical Chemistry 117 (2012) 1692–1700.

[29] M. Baneshi, S. Maruyama, H. Nakai, A. Komiya, A new approach to optimizing pigmented coatings considering both thermal and aesthetic effects, Journal of Quantitative Spectroscopy & Radiative Transfer 110 (3) (2009) 192–204.

[30] H. Gonome, M. Baneshi, J. Okajima, A. Komiya, S. Maruyama, Controlling the radiative properties of cool black-color coatings pigmented with CuO submicron particles, Journal of Quantitative Spectroscopy & Radiative Transfer 132 (2014) 90–98.

[31] J. Mora-Monteros, C. Suter, S. Haussener, Effective conductivity of porous ceramics in a radiative environment, Ceramics International 46 (2020) 2805–2815.

[32] J. Delatorre, al., Monte Carlo advances and concentrated solar applications, Solar Energy 103 (2014) 653–681.

[33] J. Krc, M. Zeman, F. Smole, M. Topie, Optical modeling of a-Si:H solar cells deposited on textured glass/ substrates, Journal of Applied Physics 92 (2) (2002) 749–755.

[34] F. Leblanc, J. Perrin, J. Schmitt, Numerical modeling of the optical properties of hydrogenated amorphoussilicon based pin solar cells deposited on rough transparent conducting oxide substrates, Journal of Applied Physics 75 (1994) 1074–1087.

[35] M. Born, E. Wolf, Principles of Optics: Electromagnetic Theory of Propagation, Interference and Diffraction of Light, cambridge university press Edition, 1999.

[36] M. Mishchenko, L. Travis, A. Lacis, Multiple Scattering of Light by Particles: Radiative Transfer and Coherent Backscattering, cambridge university press Edition, 2006.

[37] J. Howell, R. Siegel, M. Mengüç, Thermal Radiation Heat Transfer, fifth edition, CRC Press, 2010.

[38] M. Modest, Radiative Heat Transfer, second edition, Academic Press, 2003.

[39] L. Dombrovsky, D. Baillis, Thermal Radiation in Disperse Systems : an Engineering Approach, Begellhouse, 2010.

[40] W. Lipinski, J. Petrasch, S. Haussener, Application of the spatial averaging theorem to radiative heat transfer in two-phase media, Journal of Quantitative Spectroscopy & Radiative Transfer 111 (2010) 253–258.

[41] J. Randrianalisoa, S. Haussener, D. Baillis, W. Lipinski, Radiative characterization of random fibrous media with long cylindrical fibers: Comparison of single- and multi-RTE approaches, Journal of Quantitative Spectroscopy & Radiative Transfer 202 (2017) 220–232.

[42] J. Jeans, The Equations of Radiative Transfer of Energy, Monthly Notices of the Royal Astronomical Society 78 (1) (1917) 28–36.

[43] S. Chandrasekhar, Radiative Transfer, Dover Publications, 1960.

[44] P. Coelho, J. Gonçalves, Parallelization of the finite volume method for radiation heat transfer, International Journal of Numerical Methods for Heat & Fluid Flow 9 (4) (1999) 388–406.

[45] M. Badri, P. Jolivet, B. Rousseau, S. Le Corre, H. Digonnet, Y. Favennec, Vectorial finite elements for solving the radiative transfer equation, Journal of Quantitative Spectroscopy & Radiative Transfer 212 (2018) 59–74.

[46] H. Hottel, E. Cohen, Radiant heat exchange in a gas-filled enclosure: Allowance for nonuniformity of gas temperature, AIChE Journal 4 (1958) 3–14.

[47] J. Fleck, The calculation of nonlinear radiation transport by a Monte Carlo method, Technical Report UCRL- 7838, Lawrence Radiation Laboratory (1961).

[48] J. Howell, M. Perlmutter, Monte Carlo solution of thermal transfer through radiant media between gray walls, Journal of Heat Transfer 86 (1) (1964) 116–122.

[49] C. Bohren, D. Huffman, Absorption and Scattering of Light by Small Particles, john willey and sons Edition, 1983.

[50] M. Tancrez, J. Taine, Direct identification of absorption and scattering coefficients and phase function of a porous medium by a Monte Carlo technique, International Journal of Heat and Mass Transfer 47 (2004) 373–383.

[51] D. Baillis, J. Sacadura, Thermal radiation properties of dispersed media: theoretical prediction and experimental characterization, Journal of Quantitative Spectroscopy & Radiative Transfer 67 (2000) 327–363.

[52] B. Zeghondy, E. Iacona, J. Taine, Determination of the anisotropic radiative properties of a porous material by radiative distribution function identification (RDFI), International Journal of Heat and Mass Transfer 49 (2006) 2810–2819.

[53] S. Haussener, W. Lipinski, J. Petrasch, P. Wyss, A. Steinfeld, Tomographic characterization of a semitransparent-particle packed bed and determination of its thermal radiative properties, Journal of Heat Transfer 131 (2009).

[54] J. Randrianalisoa, D. Baillis, Radiative properties of densely packed spheres in semitransparent media : a new geometric optics approach, Journal of Quantitative Spectroscopy & Radiative Transfer 111 (2010) 1372–1388.

[55] M. Hale, M. Bohn, Measurement of the radiative transport properties of reticulated alumina foams, ASME-ASES Joint Solar energy Conf. OSTI :10113519 (1993).

[56] J. Kuhn, H.-P. Ebert, M. Arduini-Schuster, D. Buettner, J. Fricke, Thermal transport in polystyrene and polyurethane foam insulations, International Journal of Heat and Mass Transfer 35 (7) (1992).

[57] V. Nicolau, M. Raynaud, J. Sacadura, Spectral radiative properties identification of fiber insulating materials, Journal of Heat Transfer 37 (1994) 311–324.

[58] J.-F. Henry, C. Bissieux, S. Marquié, Y. Gillet, One-dimensional modelling and parameter estimation in scattering media, High Temperatures-High Pressures 29 (2) (1997) 159–164.

[59] P. Coray, W. Lipinski, A. Steinfeld, Spectroscopic Goniometry System for Determining Thermal Radiative Properties of Participating Media, Experimental Heat Transfer 24 (4) (2011) 300–312.

[60] D. Baillis, M. Arduini-Schuster, J. Sacadura, Identification of spectral radiative properties of polyurethane foam from hemispherical and bi-directional transmittance and reflectance measurements, Journal of Quantitative Spectroscopy & Radiative Transfer 73 (2002) 297–306.

[61] H. Davies, The reflection of electromagnetic waves from a rough surface, Proceedings of IEEE 101 (1954) 209–214.

[62] K. Torrance, E. Sparrow, Theory for off-specular reflection from roughened surfaces, Journal of the Optical Society of America 57 (9) (1967) 1105–1114.

[63] P. Beckmann, Scattering of light by rough surfaces, Progress in Optics 6 (1967) 53–69.

[64] K. Tang, R. Buckius, The geometric optics approximation for reflection from two-dimensional random rough surfaces, Journal of Heat Transfer 41 (13) (1998) 2037–2047.

[65] D. Maystre, Rigorous theory of light scattering from rough surfaces, Journal of Optics 15 (1) (1984).

[66] M. Saillard, D. Maystre, Scattering from metallic and dielectric rough surfaces, Journal of the Optical Society of America 7 (6) (1990) 982–990.

[67] H. Schade, Z. Smith, Mie Scattering and Rough Surfaces, Applied optics 24 (19) (1985) 3221–3226.

[68] P. Su, Q. Eri, Q. Wang, Optical roughness BRDF model for reverse Monte Carlo simulation of real material thermal radiation transfer, Applied optics 53 (11) (2014) 2324–2330.

[69] P. Yang, Z. M. Zhang, Bidirectional reflection of semitransparent polytetrafluoroethylene (PTFE) sheets on a silver film, International Journal of Heat and Mass Transfer 148 (2020).

[70] M. Zeman, al., Optical modeling of a-Si:H solar cells with rough interfaces: Effect of back contact and interface roughness, Journal of Applied Physics 88 (11) (2000) 6436–6443.

[71] Lai Jia Jiun, The Thermal Impact on Energy Conversion Efficiency of Thin-Film Amorphous Silicon Photovoltaic Cells, Ph.D. thesis, Swinburne University of Technology, Melbourne (2018).

[72] H. Bennett, J. Porteus, Relation Between Surface Roughness and Specular Reflectance at Normal Incidence, Journal of the Optical Society of America 51 (2) (1961) 124–130.

[73] J. Randrianalisoa, Transfert thermique par rayonnement et conduction dans les matériaux poreux, Ph.D. thesis, INSA Lyon (2006).

[74] J. Beck, V. James, K. Arnold, Parametre Estimation in Engineering and Science (Probability & Mathematical Statistics), John Wiley & Sons, 1977.